International Journal of Structural Stability and Dynamics
Vol. 21, No. 7 (2021) 2150098 (41 pages)

DOI: 10.1142/S021945542150098X

A Double Shape Memory Alloy Damper for Structural Vibration Control

Ying-Qi Jia, Chao Wang, Rui-Fu Zhang, Ling-Zhi Li*
and Zhou-Dao Lu

Department of Disaster Mitigation for Structures
Tongji University, Shanghai 200092, P. R. China
**tjlilingzhi@gmail.com*

Received 14 November 2020
Accepted 24 February 2021
Published 21 April 2021

Shape memory alloy (SMA) dampers are widely investigated passive control systems for structural vibration mitigation. However, the damping robustness of conventional austenite SMA dampers may be affected by environmental temperature. In this study, an innovative double SMA damper (DSD) system is presented to improve the temperature robustness of the SMA dampers. In the proposed system, double SMA hysteretic elements with different phase transition temperatures are arranged in parallel, where the SMA element with lower transition temperature behaves as austenite under room temperature, and the other with higher transition temperature behaves as martensite. To study the vibration control effect, both single-degree-of-freedom (SDOF) and multiple-degree-of-freedom (MDOF) structures with DSD systems are employed. The thermal and mechanical behaviors of the SMA elements and the working principle of DSD are also introduced. Thereon, the equivalent linearization method for SMA's output force and the motion-governing equations for SDOF structure with DSD are derived. Moreover, parametric studies are conducted to investigate the performance of the proposed DSD system in both frequency and time domains. Also, numerical analysis for the MDOF structure with DSD systems is carried out to illustrate the trend in response reduction with an increasing number of degrees of freedom. The analytical results show that the DSD can mitigate the structural seismic response more effectively than the conventional one with acceptable residual deformation, and is capable of delaying the degradation of SMA's energy dissipation capacity. Less SMA material is required for the proposed DSD to fulfill the same mitigation requirement, and it is suitable for general applications for temperature robustness.

Keywords: Shape memory alloy, temperature robustness, structural vibration control, structural dynamics.

1. Introduction

In recent years, frequent hazardous events (e.g. earthquakes and hurricanes) have caused numerous property damages and casualties.[1,2] The development of technologies of structural vibration control[3–6] and structure retrofit[7–10] can improve the seismic performance of structures. To mitigate the seismic response of structures, different kinds of structural control systems[11–27] have been presented by researchers all over the world, including active,[28,29] semi-active,[19,30–32] passive,[11,14,17,22–24,33] and intelligent systems.[34,35] Among these structural control systems, shape memory alloy (SMA) damper[25–27,35] has become a popularly investigated control system because of its high damping and re-centering capacities.[36,37]

As an intelligent solid–solid phase transformation material, the potential of SMA has been receiving increasing attention from scholars and engineers in the fields of aerospace and civil engineering.[26,27,37–48] Induced by temperature or stress, SMA can be transformed from one phase to another, and its shape will return to the original phase if the temperature or stress recovers to the original state (Fig. 1), which is referred to as the shape memory effect. It should be noted that if SMA is in an austenite state, the residual deformation can be eliminated,[34] and this is the well-known super-elasticity. Detailed thermal and mechanical behaviors of SMA are introduced in Sec. 2.

Considering the shape memory effect and super-elasticity, SMA can be considered as a promising energy dissipation material in the field of structural vibration control.[42,49–53] Araki *et al.*[44,54] presented a super-elastic Cu–Al–Mn SMA tensile device by employing SMAs as energy dissipating and self-centering elements, whose effectiveness was validated via experiments. Mishra *et al.*[27] presented a tuned mass damper (TMD) assisted with an SMA element based on the phase transition mechanism, which could suppress the TMD displacement more effectively with the same mass ratio of TMD to the primary structure. In addition, Wang *et al.*[37] proposed an innovative U-shaped SMA damper, whose effectiveness on structural response mitigation was also validated by experimental studies.

However, SMA-based control systems have not been widely employed in practice because of the high material costs,[53] although some recently introduced SMAs (such as Cu–Al–Mn SMA[44]) could be obtained at a lower cost. In addition, four specific obstacles keep SMA's potential from being fully utilized. (1) The lower fracture level (short fatigue life) of some SMAs is unsatisfactory to employ for vibration control of structures suffering frequent oscillations. For example, 100,000 working cycles of SMAs in stayed cables are expected for wind-resistance each day, whereas fatigue fracture will occur in Cu–Al–Be SMA under 2000 cycles (although it is acceptable for

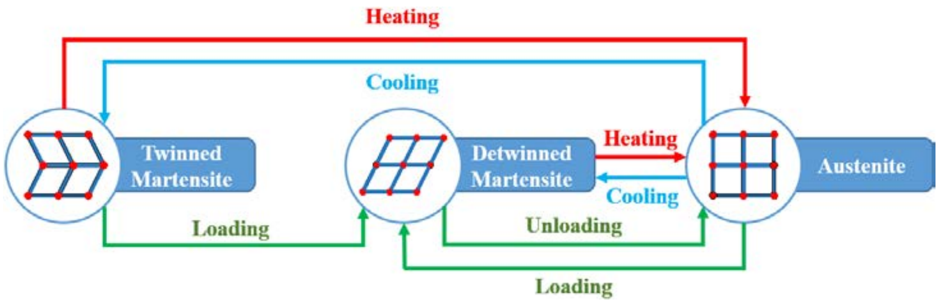

Fig. 1. Phase transition diagram of SMA.

anti-earthquake dampers).[55] (2) SMA elements might experience buckling under compressive loads, which may result in a poor energy dissipation effect of SMA-based control systems. (3) There is a design contradiction between the large SMA deformation (positively correlated with the capacity of energy dissipation) and the small structural displacement.[35] (4) SMA is highly sensitive to the environmental temperature[41,55] and the seasonal temperature effect (i.e. seasonal temperature between winter and summer could modify the shape of SMAs hysteresis loop) may result in damper failure.

Under this circumstance, many scholars have devoted themselves to addressing these issues and improving the performance of SMA-based control systems. In terms of issue (1), more adaptive types of SMAs (such as Ni–Ti SMA[55]) could be employed in situations where frequent and long-duration oscillations occur. Regarding issue (2), many novel devices have been put forward to overcome this difficulty from the perspective of mechanics.[37,46,54] In these works, SMA elements are subjected to tensile strain all the time, regardless of structural moving direction. As for issue (3), Jia *et al.*[35] proposed an SMA damping inerter to fully utilize the damping potential of SMA by introducing a two-terminal inerter element[2,23,56] to enlarge the SMA deformation. By this means, the system's ability to dissipate seismic energy is enhanced, indicating that a lower SMA material cost is required to fulfill the same structural response mitigation requirement. Concerning issue (4), only certain references[36,41,55] have presented that SMA's damping capacity degrades as the temperature increases. Considering that the ambient temperature of structures could vary dozens of Celsius degrees in a given region in a year, especially in high-altitude regions, it is of great importance to enhance the temperature robustness for SMA-based dampers, which is the main target of this work.

Therefore, to improve the temperature robustness of SMA dampers, this study presents an innovative double SMA damper (DSD) system, which employs two hysteretic SMA elements with different phase transition temperatures. In Sec. 2, the analytical models of DSD-fitted single-degree-of-freedom (SDOF) structures, the constitutive behaviors of SMA elements, and the working principle of the DSD system are introduced. In Sec. 3, the equivalent linearization method for SMA's output force and the motion-governing equations are given. In Sec. 4, parametric studies for DSD's performance are implemented. To verify DSD's effectiveness, frequency-domain and time-domain analyses are given in Sec. 5. On top of that, the theoretical and numerical analyses for multiple-degree-of-freedom (MDOF) structures with DSD systems are given in Sec. 6 to illustrate the extensibility of the proposed system. Finally, conclusions are drawn in Sec. 7.

2. Outline of a DSD System

2.1. *Analytical models for DSD-fitted structures*

As shown in Fig. 2(a), an analytical model of an SDOF structure with a DSD system is employed to investigate DSD's performance. The SDOF structure adopted in this

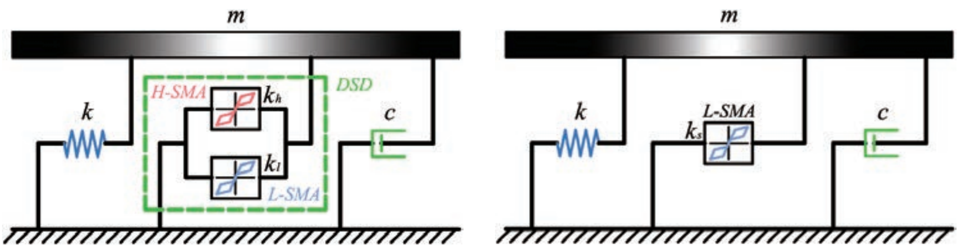

(a) With DSD

(b) With a conventional SMA damper

Fig. 2. Analytical models of SDOF structures installed with (a) DSD and (b) a conventional SMA damper.

study consists of a structural mass m, a linear structural spring part k, and structural damping c. In the proposed DSD system, two SMA hysteretic elements with different phase transition temperatures are arranged in parallel. The SMA element with lower phase transition temperatures is referred to as L-SMA, and the other with higher phase transition temperatures is referred to as H-SMA, whose initial stiffness coefficients are denoted as k_l and k_h, respectively. It should be noted that, under room temperature, the L-SMA in DSD behaves as austenite while the H-SMA element behaves as martensite. A conventional austenite SMA damper that consists of an L-SMA element with initial stiffness k_s is also utilized as a comparison to DSD (as shown in Fig. 2(b)).

Considering that the phase transition temperatures of SMA range from minus dozens to a thousand Celsius degrees,[40,57] the commonly used Ni–Ti SMA,[58] is employed and set with reasonable but different phase transition temperatures to generate L-SMA and H-SMA, whose default values of parameters are shown in Table 1. D_A and D_M are elastic moduli of austenite and martensite phases, respectively. Θ is related to the thermal coefficient of expansion of SMA, and ε_l is the maximum residual strain. C_M and C_A are material properties, which describe the relationship between the temperature and critical stress values (σ_s^{cr} and σ_f^{cr}). M_f, M_s, A_s, and A_f are four vital phase transition temperatures of SMA, which represent martensite finish, martensite start, austenite start, and austenite finish transition temperatures, respectively, and satisfy the relation of $M_f < M_s < A_s < A_f$.

Table 1. Default values of parameters of L-SMA and H-SMA elements.

Thermodynamic parameters	Transition parameters	Transition temperatures of L-SMA	Transition temperatures of H-SMA
$D_A = 67000\,\mathrm{MPa}$	$C_M = 8\,\mathrm{MPa}/^\circ\mathrm{C}$	$M_{fl} = -41.7^\circ\mathrm{C}$	$M_{fh} = -26.0^\circ\mathrm{C}$
$D_M = 26300\,\mathrm{MPa}$	$C_A = 13.8\,\mathrm{MPa}/^\circ\mathrm{C}$	$M_{sl} = -37.2^\circ\mathrm{C}$	$M_{sh} = -16.6^\circ\mathrm{C}$
$\Theta = 0.55\,\mathrm{MPa}/^\circ\mathrm{C}$	$\sigma_s^{\mathrm{cr}} = 300\,\mathrm{MPa}$	$A_{sl} = -27.3^\circ\mathrm{C}$	$A_{sh} = -0.5^\circ\mathrm{C}$
$\varepsilon_l = 0.067$	$\sigma_f^{\mathrm{cr}} = 400\,\mathrm{MPa}$	$A_{fl} = -19.1^\circ\mathrm{C}$	$A_{fh} = 14.0^\circ\mathrm{C}$

Notes: Subscripts l and h represent L-SMA and H-SMA, respectively.

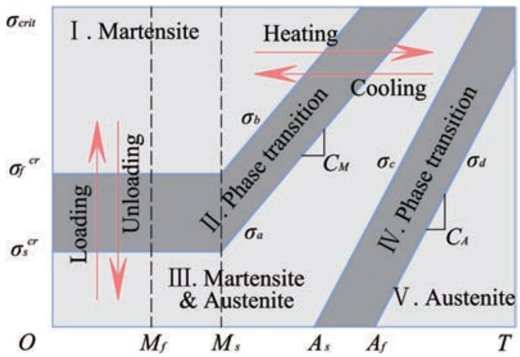

Fig. 3. Phase diagram of martensite and austenite transformations of SMA.

2.2. *Thermal and mechanical behaviors of SMAs*

As mentioned above, SMA can be transformed from one phase to another when induced by temperature or stress. This complex relationship of the SMA phase transition can be illustrated with the phase diagram[59] as shown in Fig. 3, in which the temperature T is on the x-axis and the critical stress σ_{crit} is on the y-axis. σ_s^{cr} and σ_f^{cr} are critical stresses when the martensite transformation starts and finishes subjected to the condition of $T < M_s$, respectively. In the diagram, σ_a, σ_b, σ_c, and σ_d are four critical stress lines dividing the phase diagram into five regions. SMA located in Region I, III, and V behaves as pure martensite, the coexistence of martensite and austenite, and pure austenite, respectively. Under the effects of loading, unloading, heating, or cooling, the state of SMA can cross Region II or IV to achieve the phase transition. Considering the temperature has a great effect on SMA's phase transition, constitutive behaviors of SMA are discussed in the following sections by classifying the temperature into three categories: $T < A_s$, $A_s < T < A_f$, and $T > A_f$.

2.2.1. *Constitutive behavior of SMA subjected to $T < A_s$*

As for SMA subjected to $T < A_s$ shown in Fig. 4, SMA is subjected to the elastic deformation in the state of coexistence of martensite and austenite or pure martensite from O to A (A'). The slope of the line OA (OA') is denoted as k_1. The direction of the skeleton curve changes at point A (A'), which is analogous to the yielding point of the steel. From A (A') to B (B'), the displacement of SMA increases substantially, and a further increase of load makes SMA break. The slope of the line AB ($A'B'$) is denoted as k_2. SMA is completely transformed into stress-induced pure martensite at point B (B'). Unloading from point B (B') to E (E'), a small part of strain is recovered (the residual strain can be fully eliminated after heating SMA owing to the shape memory effect), and the slope of the line BE ($B'E'$) is denoted as k_3. Finally, reverse loading begins.

According to the theory given by Du *et al.*,[58] coordinates of the characteristic points in Fig. 4 are shown in Table 2, where S and L are the cross-sectional area and

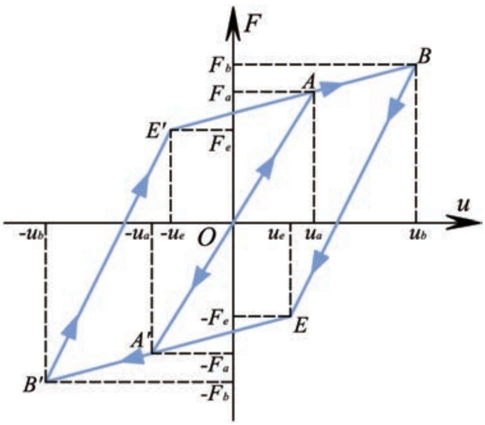

Fig. 4. Constitutive behavior of SMA subjected to $T < A_s$.

Table 2. Coordinates of the characteristic points of the constitutive behavior of SMA subjected to $T < A_s$.

Load	Displacement	Stiffness
$F_a = [\sigma_s^{\mathrm{cr}} + \Gamma(T - M_s)C_M(T - M_s)]S$	$u_a = F_a L/D_M S$	$k_1 = [D_A(1-\xi) + D_M \xi]S/L$
$F_b = [\sigma_f^{\mathrm{cr}} + \Gamma(T - M_s)C_M(T - M_s)]S$	$u_b = (F_b/D_M S + \varepsilon_L)L$	$k_2 = (F_b - F_a)/(u_b - u_a)$
$F_e = k_2(u_e + u_b) - F_b$	$u_e = [2F_b - (k_2 + k_3)u_b]/(k_2 - k_3)$	$k_3 = D_M S/L$

the length of the equivalent elastic rod of the SMA element, respectively. ξ is the proportion of martensite in SMA. In this study, SMA in Fig. 4 is assumed to be pure martensite in its initial state for convenience (i.e. $\xi = 1$ and $k_1 = D_M S/L$). $\Gamma(T - M_s)$ is a unit step function defined as

$$\Gamma(T - M_s) = \begin{cases} 1, & \text{if } T \geq M_s \\ 0, & \text{if } T < M_s \end{cases}. \tag{1}$$

2.2.2. *Constitutive behavior of SMA subjected to $A_s < T < A_f$*

Brinson[59] presented that martensite and austenite could coexist in SMA when the temperature is between A_s and A_f, and SMA's displacement could be recovered partially after unloading (as shown in Fig. 5(a)). Considering most of the SMA deformation is concentrated in the zone with low values (shadow area in Fig. 5), the force–deformation behavior in this stage could be simplified by ignoring the partial displacement recovery (Fig. 5(b)). That is, the constitutive behavior of SMA subjected to $A_s < T < A_f$ is assumed to be the same as SMA subjected to $T < A_s$.

2.2.3. *Constitutive behavior of SMA subjected to $T > A_f$*

In terms of SMA subjected to $T > A_f$ as shown in Fig. 6, from O to A (A'), SMA is subjected to the elastic deformation in a pure austenite state. The slope of the line OA (OA') is denoted as k_1. SMA begins to be transformed into martensite at point

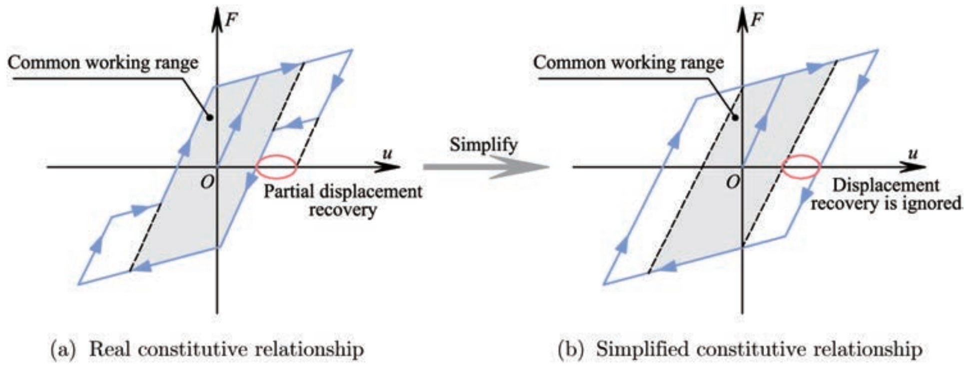

Fig. 5. Constitutive behavior of SMA subjected to $A_s < T < A_f$.

A (A') and will be completely transformed into stress-induced pure martensite at point B (B'), in which state the SMA displacement increases greatly and the load increases slowly. The slope of the line AB ($A'B'$) is denoted as k_2. Further increase of load makes SMA elongate elastically, which is not shown as the displacement exceeding u_b is ignored in the design for conservation reasons.

Unloading from the point B (B') to C (C'), the strain is recovered elastically in a pure martensite state, and the slope of the line BC ($B'C'$) is denoted as k_3. Subsequently, from point C (C') to D (D'), SMA is transformed from martensite to austenite rapidly, and the strain is recovered substantially. The slope of the line CD ($C'D'$) is denoted as k_4. Finally, SMA is elastically recovered to the initial state in the pure austenite phase, and reverse loading begins. Coordinates of the characteristic points[58] in Fig. 6 are shown in Table 3.

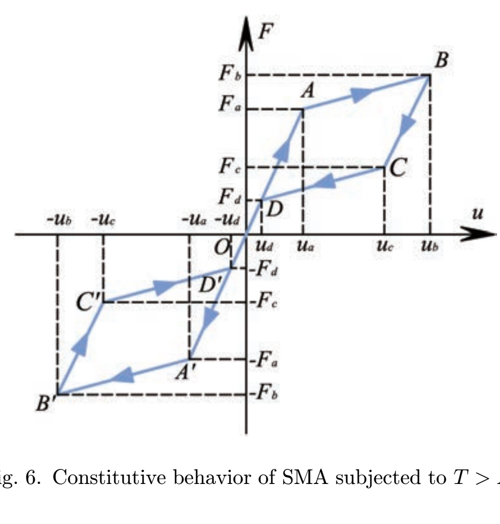

Fig. 6. Constitutive behavior of SMA subjected to $T > A_f$.

Table 3. Coordinates of the characteristic points of the constitutive behavior of SMA subjected to $T > A_f$.

Load	Displacement	Stiffness
$F_a = [\sigma_s^{cr} + C_M(T - M_s)]S$	$u_a = F_a L/D_A$	$k_1 = D_A S/L$
$F_b = [\sigma_f^{cr} + C_M(T - M_s)]S$	$u_b = (F_b/D_M S + \varepsilon_l)L$	$k_2 = (F_d - F_b)/(u_b - u_d)$
$F_c = C_A(T - A_s)S$	$u_c = u_d + (F_c - F_d)L/D_M S$	$k_3 = D_M S/L$
$F_d = C_A(T - A_f)S$	$u_d = F_d L/D_A$	$k_4 = (F_c - F_a)/(u_c - u_a)$

2.3. *Working principle of the DSD system*

2.3.1. *Degradation of SMA's energy dissipation capacity*

Before illustrating the working principle of the DSD system, it is necessary to display how SMA's energy dissipation capacity degrades with the temperature increasing. According to the one-dimensional constitutive behavior of SMA proposed by Brinson,[59] the constitutive relationship of SMA (L-SMA is utilized here as an example) under varying temperatures ranging from $-10°$C to $40°$C can be derived programmatically with Matlab (shown in Fig. 7). It can be observed that with the increasing temperature, the yielding point moves up to the right and the hysteretic loop becomes smaller. In addition, according to these constitutive relationships, the areas of their hysteretic loops can be calculated (shown in Fig. 8), which represent the capacity of SMA's hysteretic energy dissipation (in the form of strain energy).[60] It could be seen that the energy dissipation capacity decreases by 62.5% with the temperature increasing from $-10°$C to $40°$C. Therefore, a conventional SMA damper could only perform well in a narrow temperature range (such as the room temperature),[27] and its performance will degrade significantly under higher temperatures. Therefore, it is of great significance to study the feasibility of the DSD system that may work well under varying temperatures and replace the conventional one.

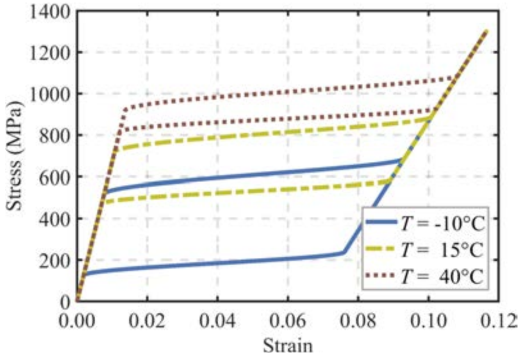

Fig. 7. Constitutive relationship under varying temperatures ranging from $-10°$C to $40°$C.

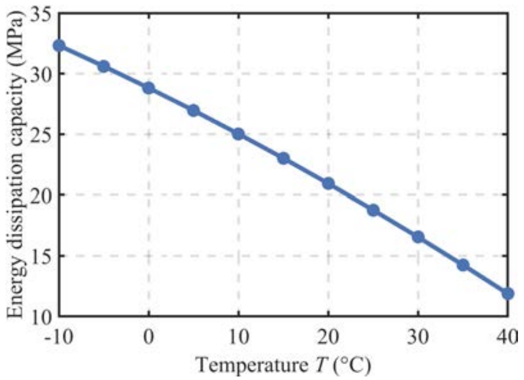

Fig. 8. Relationship between SMA's energy dissipation capacity and temperature.

2.3.2. *Working principle of the DSD system*

With aforementioned analyses, hysteresis loops of three different types of SMA dampers, i.e. SMA damper composed of H-SMA element, SMA damper composed of L-SMA element, and DSD composed of both L-SMA and H-SMA elements, are shown in Fig. 9, where three typical ambient temperatures of buildings ($-10°$C, $15°$C, and $40°$C) are considered. The skeleton curves of the SMA damper with the H-SMA element are shown in Fig. 9(a). When the temperature is lower than the austenite finish temperature of H-SMA ($A_{fh} = 14°$C), H-SMA is transformed into martensite, and SMA damper with H-SMA will remain a large residual deformation

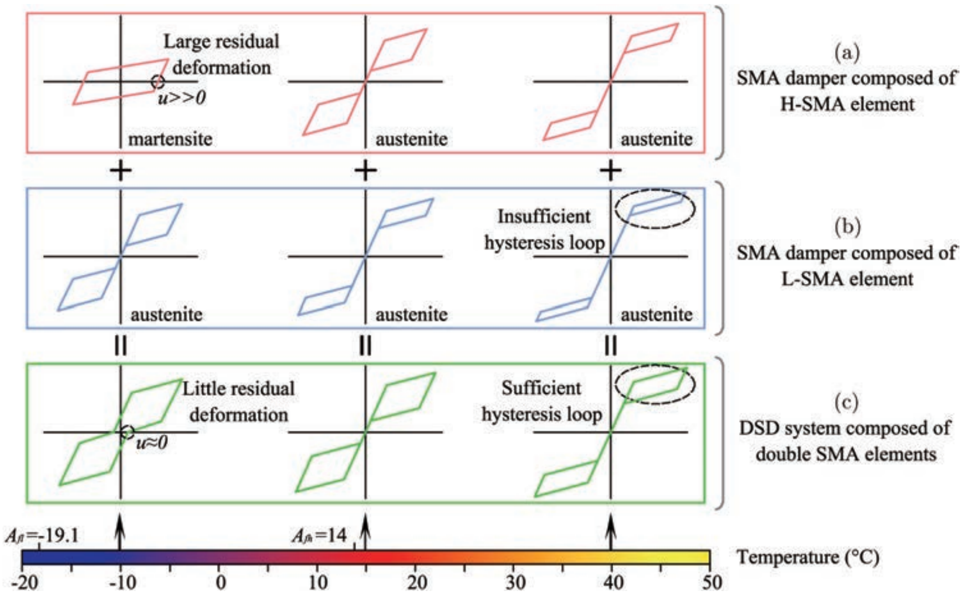

Fig. 9. The variations of the shapes of SMA's hysteresis loops under varying temperatures.

under seismic excitation. For this reason, this type of SMA damper has not received too much research interest from scholars.

Moreover, the skeleton curves of the SMA damper with the L-SMA element under different temperatures are shown in Fig. 9(b). L-SMA is transformed into austenite when the temperature is higher than the austenite finish temperature of L-SMA (A_{fl}=−19.1°C), and an insufficient hysteresis loop will occur with the temperature increasing. As presented in the previous section, the energy dissipation capacity of the SMA element decreases with the temperature increasing (Fig. 8), which limits the application of the SMA damper with the L-SMA element in structures under higher temperatures.

As shown in Fig. 9(c), for the proposed DSD system, the area of the hysteresis loop is sufficient, and the residual deformation is negligible in a wide range of temperatures from −10°C to 40°C. Thus, the combination of advantages of H-SMA and L-SMA elements can be realized in DSD, for it remains negligible residual deformation owing to the super-elasticity of L-SMA and shows sufficient hysteresis loop owing to the compensation effect of H-SMA. Therefore, satisfactory temperature robustness on structural response mitigation can be achieved in the DSD system by employing double SMA hysteretic elements with different phase transition temperatures.

3. Problem Formulation

3.1. *Output force of SMA elements in DSD*

The solution of structural seismic response presented in this work is nonlinear due to the hysteresis characteristics of SMA elements. Hence, it is of great importance to employ an appropriate method to simplify the output forces of SMA elements in the DSD system. The one-dimensional piecewise linear model given by Du *et al.*[58] can reflect the influence of temperature on the force–deformation behavior of SMA. However, the loading and unloading paths within the hysteretic loop given by this model are too sophisticated to use in the stochastic vibration analysis. Moreover, the Bouc–Wen model[61] (a general hysteresis model) and Graesser–Cozzaralli model[62] (an SMA hysteresis model presented based on the former) can be used to describe the geometric shape of the constitutive curve. Nevertheless, the physical meanings of these models' parameters are unclear and their expressions are given in complicated nonlinear and differential forms, which are also too complicated to use in structural dynamic analysis. Subsequently, a simplified equation of the austenite SMA's output force was proposed by Yan and Nie,[60] which can be expressed as

$$\begin{cases} F_d = \alpha_d k_d x + (1-\alpha_d) k_d z_d. \\ z_d = [1 - \mathrm{sign}\{\mathrm{sign}(|x| - u_a) + 1\}]x \\ \qquad + \dfrac{\mathrm{sign}(|x| - u_a) + 1}{2}\left[(u_b - u_a)\dfrac{\mathrm{sign}(x) + \mathrm{sign}(\dot{x})}{2} + u_a \mathrm{sign}(x)\right] \end{cases}, \quad (2)$$

where F_d is the simplified SMA's output force. k_d is the initial stiffness, and α_d is the stiffness ratio of the post- to pre-yielding. x and z_d are the overall and hysteretic displacements of SMA, respectively. sign(x) is a mathematical function defined as

$$\mathrm{sign}(x) = \begin{cases} 1, & \text{if } x > 0 \\ 0, & \text{if } x = 0 \\ -1, & \text{if } x < 0 \end{cases}. \tag{3}$$

Although a relatively simplified expression of the SMA element's output force is given in Eq. (2), it is still nonlinear and inconvenient to employ in the structural dynamics directly. Many analytical methods have been developed to further simplify this kind of nonlinear problem, such as the stationary FPK equation method,[63] equivalent linearization method,[64] equivalent nonlinear system method,[65] and Monte Carlo method.[66] Among these analytical methods, the equivalent linearization method is a robust tool owing to its concise expressions and explicit physical meanings of parameters. According to certain rules, the nonlinear output force can be replaced by a linear one. Yan and Nie[60] further employed this equivalent linearization method to obtain the linear form of Eq. (2), which is widely used in the field of structural vibration control and restated in the following subsection.

3.1.1. *Equivalent linearization for austenite SMA*

As proposed by Yan and Nie,[60] the equivalent form of SMA's hysteretic displacement is denoted as

$$\bar{z}_d = k_e x + c_e \dot{x}, \tag{4}$$

where k_e and c_e are two coefficients that will be determined later.

Substituting Eq. (4) in Eq. (2), the equivalent form of the output force can be expressed as

$$F_d = \alpha_d k_d x + (1 - \alpha_d) k_d (k_e x + c_e \dot{x}) = \tilde{k}_e x + \tilde{c}_e \dot{x}, \tag{5}$$

where $\tilde{k}_e$ and $\tilde{c}_e$ are stochastically equivalent stiffness and damping coefficients, respectively, and given as

$$\tilde{k}_e = \alpha_d k_d + (1 - \alpha_d) k_d k_e, \quad \tilde{c}_e = (1 - \alpha_d) k_d c_e. \tag{6}$$

To achieve satisfactory equivalent linearization, the condition to guarantee the least square error between the linearized $\bar{z}_d$ and nonlinear z_d items should be satisfied. According to the first-order condition, the requirements that the square error $\mathrm{E}[(\bar{z}_d - z_d)^2] = \mathrm{E}[(k_e x + c_e \dot{x} - z_d)^2]$ takes the minimum value are

$$\frac{\partial \mathrm{E}[(\bar{z}_d - z_d)^2]}{\partial k_e} = 0, \quad \frac{\partial \mathrm{E}[(\bar{z}_d - z_d)^2]}{\partial c_e} = 0, \tag{7}$$

where E[ ] represents the expectation operator.

Solving Eq. (7) with respect to k_e and c_e, we obtain

$$k_e = \frac{\mathrm{E}[x(t)z_d(t)]}{\mathrm{E}[x(t)^2]}, \quad c_e = \frac{\mathrm{E}[\dot{x}(t)z_d(t)]}{\mathrm{E}[\dot{x}(t)^2]}. \tag{8}$$

Then, substituting z_d in Eq. (2) into Eq. (8), k_e and c_e can be further expressed as

$$k_e = \frac{u_b + u_a}{\sqrt{2\pi}\sigma_x}\mathrm{e}^{-\frac{u_a^2}{2\sigma_x^2}}, \quad c_e = \frac{u_b - u_a}{\sqrt{2\pi}\sigma_{\dot{x}}}\left[1 - \mathrm{erf}\left(\frac{u_a}{\sqrt{2}\sigma_x}\right)\right], \tag{9}$$

where σ_x and $\sigma_{\dot{x}}$ are standard deviations of x and $\dot{x}$, respectively. $\mathrm{erf}(x)$ is the error function defined as

$$\mathrm{erf}(x) = \frac{2}{\sqrt{\pi}}\int_0^x \mathrm{e}^{-\eta^2}d\eta. \tag{10}$$

Finally, substituting Eq. (9) into Eq. (6), stochastically equivalent stiffness and damping can be expressed as

$$\begin{aligned} \tilde{k}_e &= \alpha_d k_d + (1-\alpha_d)k_d\frac{u_b + u_a}{\sqrt{2\pi}\sigma_x}\mathrm{e}^{-\frac{u_a^2}{2\sigma_x^2}}, \\ \tilde{c}_e &= (1-\alpha_d)k_d\frac{u_b - u_a}{\sqrt{2\pi}\sigma_{\dot{x}}}\left[1 - \mathrm{erf}\left(\frac{u_a}{\sqrt{2}\sigma_x}\right)\right]. \end{aligned} \tag{11}$$

3.1.2. *Equivalent linearization for martensite SMA*

As for martensite SMA, the bilinear model[67] can be utilized to model the hysteretic displacement, and then the output force of martensite SMA can be expressed as

$$\begin{cases} F_d = \alpha_d k_d x + (1-\alpha_d)k_d z_d \\ z_d = u_a \mathrm{sign}(\dot{x}). \end{cases} \tag{12}$$

Similar to the equivalent linearization method employed for austenite SMA, k_e and c_e for martensite SMA can be obtained as

$$k_e = 0, \quad c_e = \sqrt{\frac{2}{\pi}}\frac{u_a}{\sigma_{\dot{x}}}. \tag{13}$$

Substituting Eq. (13) into Eq. (6), stochastically equivalent stiffness and damping coefficients of martensite SMA can be expressed as

$$\tilde{k}_e = \alpha_d k_d, \quad \tilde{c}_e = (1-\alpha_d)k_d\sqrt{\frac{2}{\pi}}\frac{u_a}{\sigma_{\dot{x}}}. \tag{14}$$

Considering the high degree of nonlinearity involved in this study, the analytical result of the stochastic response can be derived conveniently in the following sections by employing Eqs. (5), (11), and (14). It should be noted that the aforementioned linear forms of output force can still maintain the nonlinear characteristics of SMA, since $\tilde{k}_e$ and $\tilde{c}_e$ are related to statistics (σ_x and $\sigma_{\dot{x}}$) of random variables (x and $\dot{x}$).

3.2. *Motion-governing equations for DSD-fitted structures*

According to the above equivalent linearization method, the SMA elements in DSD are equivalent to the combination of a supporting spring with stiffness $\tilde{k}_e$ and an energy dissipation element with a damping coefficient $\tilde{c}_e$. Therefore, the analytical model of the SDOF structure with DSD shown in Fig. 2(a) can be replaced with the equivalent form shown in Fig. 10. It can be observed that L-SMA in DSD is replaced by a supporting spring $\tilde{k}_{el}$ and an energy dissipation element $\tilde{c}_{el}$. Similarly, the respective supporting spring and the energy dissipation element for H-SMA are denoted as $\tilde{k}_{eh}$ and $\tilde{c}_{eh}$, respectively.

The motion-governing equation for the SDOF structure assisted with a DSD system subjected to the ground motion can be written as

$$m\ddot{x} + c\dot{x} + kx + F_s(x, \dot{x}) = -m\ddot{x}_g, \tag{15}$$

where x is the displacement of the primary structure with respect to the ground. The velocity and acceleration are given by $\dot{x}$ and $\ddot{x}$, respectively. The ground acceleration of the earthquake is represented by $\ddot{x}_g$. As presented in the previous section, the overall output force F_s of DSD can be expressed as

$$F_s(x, \dot{x}) = \tilde{c}_{el}\dot{x} + \tilde{k}_{el}x + \tilde{c}_{eh}\dot{x} + \tilde{k}_{eh}x. \tag{16}$$

Substituting Eq. (16) into Eq. (15), we obtain

$$m\ddot{x} + (c + \tilde{c}_{el} + \tilde{c}_{eh})\dot{x} + (k + \tilde{k}_{el} + \tilde{k}_{eh})x = -m\ddot{x}_g. \tag{17}$$

Then the well-known Kanai–Tajimi stochastic model[68] could be utilized to obtain the stationary ground motion, which filters a white noise process acting on the rock bed. Kanai–Tajimi stochastic model is expressed as

$$\begin{cases} \ddot{x}_f + 2\xi_f\omega_f\dot{x}_f + \omega_f^2 x_f = -\ddot{w} \\ \ddot{x}_g = -2\xi_f\omega_f\dot{x}_f - \omega_f^2 x_f \end{cases}, \tag{18}$$

where ξ_f and ω_f are damping coefficient and frequency of the soil strata, respectively. $\ddot{w}$ is the white noise intensity of the rock bed with the power spectral density S_0. $\ddot{x}_f$, $\dot{x}_f$, and x_f are the acceleration, velocity, and displacement responses of the soil

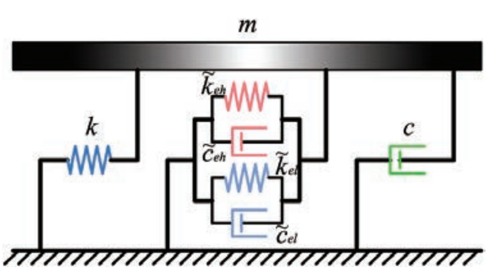

Fig. 10. Equivalent form of SDOF structure with DSD.

filter, respectively. The state vector for the DSD-fitted structure can be defined as

$$\mathbf{u} = \{x, x_f, \dot{x}, \dot{x}_f\}^{\mathrm{T}}. \tag{19}$$

Then the motion-governing equation given in Eq. (15) could be written in the state space form as

$$\frac{\mathrm{d}\mathbf{u}}{\mathrm{d}t} = \mathbf{A}\mathbf{u} + \mathbf{w}, \tag{20}$$

where $\mathbf{w} = \{0\ 0\ 0\ -\ddot{w}\}^{\mathrm{T}}$ is a vector that contains the intensity of the white noise, and $\mathbf{A}$ is an augmented matrix expressed as

$$\mathbf{A} = \begin{bmatrix} 0 & 0 & 1 & 0 \\ 0 & 0 & 0 & 1 \\ -(k + \tilde{k}_{el} + \tilde{k}_{eh})/m & \omega_f^2 & -(c + \tilde{c}_{el} + \tilde{c}_{eh})/m & 2\xi_f\omega_f \\ 0 & -\omega_f^2 & 0 & -2\xi_f\omega_f \end{bmatrix}. \tag{21}$$

Assuming that the responses are stationary and Markovian, the evolution equation (Lyapunov equation) could be obtained as[62]

$$\frac{\mathrm{d}\mathbf{C}_{uu}}{\mathrm{d}t} = \mathbf{A}\mathbf{C}_{uu} + \mathbf{C}_{uu}\mathbf{A}^{\mathrm{T}} + \mathbf{S}_{ww} = 0, \tag{22}$$

where $\mathbf{C}_{uu}$ is the covariance matrix of the state vector $\mathbf{u}$, and $\mathbf{S}_{ww}$ is the input matrix of the excitation of the rock bed, which can be written as

$$\mathbf{C}_{uu} = \begin{bmatrix} \sigma_x^2 & \sigma_{xx_f} & \sigma_{x\dot{x}} & \sigma_{x\dot{x}_f} \\ & \sigma_{x_f}^2 & \sigma_{x_f\dot{x}} & \sigma_{x_f\dot{x}_f} \\ & & \sigma_{\dot{x}}^2 & \sigma_{\dot{x}\dot{x}_f} \\ \text{sym.} & & & \sigma_{\dot{x}_f}^2 \end{bmatrix}, \quad \mathbf{S}_{ww} = \begin{bmatrix} 0 & & & \\ & 0 & & \\ & & 0 & \\ & & & 2\pi S_0 \end{bmatrix}. \tag{23}$$

Then the structural and DSD's responses can be solved with continuous iterations until the convergence of $\mathbf{C}_{uu}$.

4. Parametric Study

4.1. *Stochastic performance indicators of DSD*

As presented earlier, DSD is mainly composed of two SMA hysteretic elements: H-SMA and L-SMA. As for a single SMA hysteretic element, the output force is determined by the initial stiffness (k_l or k_h), characteristic displacements (u_a and u_b shown in Fig. 4 or Fig. 6), and environmental temperature T. The initial stiffness can be represented by another two physical parameters κ_l and κ_h, which are commonly used in structural control theories and restated here as[27]

$$\kappa_l = k_l/k, \quad \kappa_h = k_h/k. \tag{24}$$

Then three stochastic performance indicators of DSD can be defined as follows:

(1) To analyze the damping effect of DSD under a given temperature T, a dimensionless quantity referred to as structural response mitigation ratio[2] is defined as

$$\bar{\sigma}_x = \sigma_x/\sigma_x^{uc}, \tag{25}$$

where σ_x and σ_x^{uc} are the root-mean-square (RMS) displacements of the controlled and uncontrolled structures, respectively.

(2) Moreover, the residual deformation is another important indicator representing DSD's self-centering ability and is given as

$$u_{\text{res}} = \max\{\text{abs}\{x|F_s(x) = 0\}\}. \tag{26}$$

(3) In addition, the efficient tuning bandwidth of frequency is also an essential indicator, which represents the robustness of the damping effect under seismic excitation with different frequency components. According to the concept of the efficient tuning bandwidth of frequency,[69] it can be defined as

$$\begin{cases} w = \max(B) - \min(B) \\ B = \{\omega|S_u(\omega) \leq S_u^{uc}(\omega)\} \end{cases}, \tag{27}$$

where B is the range of the efficient tuning frequency of DSD, and w is the bandwidth of B. $S_u(\omega)$ and $S_u^{uc}(\omega)$ are the displacement power spectral density functions (PSDFs, in $\text{m}^2 \cdot \text{s}$) of the controlled and uncontrolled structures, respectively. ω is the frequency (in rad/s) of the seismic excitation.

Hence, the problem of parametric analysis can be summarized as

$$\{\kappa_l, \kappa_h, u_{al}, u_{bl}, u_{ah}, u_{bh}, T\} \rightarrow \{\bar{\sigma}_x, u_{\text{res}}, w\}, \tag{28}$$

where u_{ah}, u_{bh}, u_{al}, and u_{bl} are the characteristic displacements of H-SMA and L-SMA, respectively. According to expressions in Tables 2 and 3, u_{al}, u_{bl}, u_{ah} and u_{bh} are functions of the temperature T if a given length $L \equiv 4\,\text{m}$ is assumed, and then the problem of parametric analysis can be further simplified as

$$\{\kappa_l, \kappa_h, T\} \rightarrow \{\bar{\sigma}_x, u_{\text{res}}, w\}. \tag{29}$$

For a parametric study, a reasonable range of the κ_l and κ_h is given as $[10^{-2}, 10^1]$ in Ref. 2 and three typical values of T (namely, -10°C, 15°C, and 40°C) are utilized to simulate different temperature conditions. The stiffness ratio of the conventional SMA damper ($\kappa_s = k_s/k$) is assumed to be the same as the sum of κ_l and κ_h (i.e. $\kappa_s = \kappa_l + \kappa_h$). The default values of parameters for the primary structure and soil strata are the same as the data provided by Ref. 27, as shown in Table 4.

Table 4. Default values of parameters of the primary structure and soil strata.

Mass	Period	Damping ratio	Power spectrum density	Damping	Frequency
$m = 200$ ton	$T_s = 1.5\,\text{s}$	$\xi = 0.03$	$S_0 = 0.05\,\text{m}^2/\text{s}^3$	$\zeta_g = 0.6$	$\omega_g = 9\pi\,\text{rad/s}$

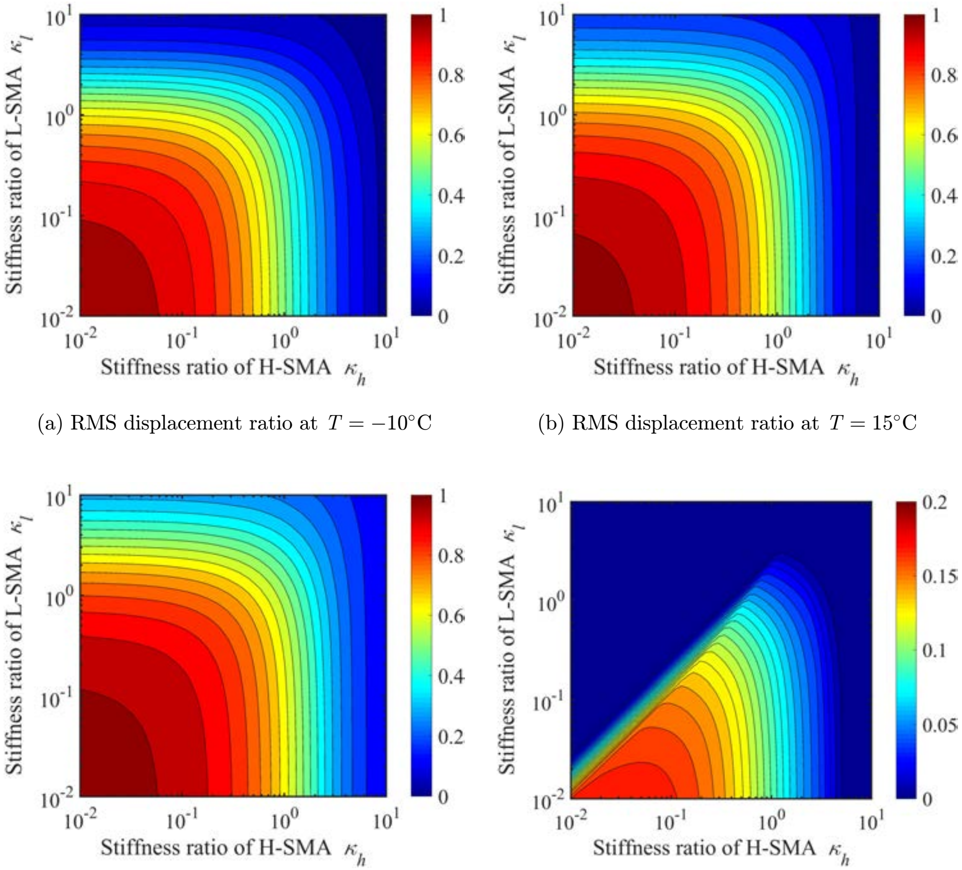

(a) RMS displacement ratio at $T = -10°\mathrm{C}$

(b) RMS displacement ratio at $T = 15°\mathrm{C}$

(c) RMS displacement ratio at $T = 40°\mathrm{C}$

(d) Residual deformation at $T = -10°\mathrm{C}$

Fig. 11. Contour plots of the RMS displacement ratios ((a)–(c)) and residual deformation (d) of the SDOF structure with different DSD systems for $\kappa_l \in [10^{-2}, 10^1]$ and $\kappa_h \in [10^{-2}, 10^1]$ under varying temperatures.

4.2. *Structural response mitigation ratio* $\bar{\sigma}_x$ *and residual deformation* u_{res}

As shown in Figs. 11(a)–11(c), a series of contour plots are displayed with κ_h on the x-axis, κ_l on the y-axis, and $\bar{\sigma}_x$ as the height. Some information can be observed from the figures: (1) A decrease in $\bar{\sigma}_x$ is accompanied by increases in κ_h and κ_l, and there are optimal damping areas located in the upper-right corners for each parameter sets. (2) With the temperature T increasing, the optimal damping area is gradually becoming slender, indicating that the structural damping effect of DSD degrades with the increasing temperature T.

As shown in Fig. 11(d), u_{res} is the height of the contour plot and several conclusions can be obtained: (3) No matter how large κ_l is, the residual deformation of DSD is negligible when the value of κ_h is very low, as all the residual deformation of DSD results from H-SMA and a superior self-centering capacity could be provided by L-SMA. (4) The most unfavorable deformation region is in the lower-middle part of Fig. 11(d), where the κ_l is inadequate to supply sufficient self-centering capacity for DSD. Meanwhile, greater κ_h will reduce the residual deformation as a greater stiffness is imposed on the primary structure, and fewer κ_h will also weaken the residual deformation since H-SMA is the only source that could induce the residual deformation. Considering observations (1)–(4), the ideal parameter settings for acceptable damping effects are estimated as $\kappa_l \in [0.3, 0.9]$ and $\kappa_h \in [0.2, 0.8]$.

4.3. *Efficient tuning bandwidth of the frequency w*

To investigate the efficient tuning bandwidth of frequency of DSD under varying temperatures, PSDFs of the SDOF structures with different DSDs are shown in Figs. 12–14. The driving frequency ω is on the x-axis and PSDFs are on the y-axis. The ranges of κ_l and κ_h are, respectively, selected as $\kappa_l \in [0.3, 0.9]$ and $\kappa_h = [0.2, 0.8]$ according to the above-mentioned analyses. According to Eq. (27), values of efficient bandwidth w can be calculated and shown in Table 5.

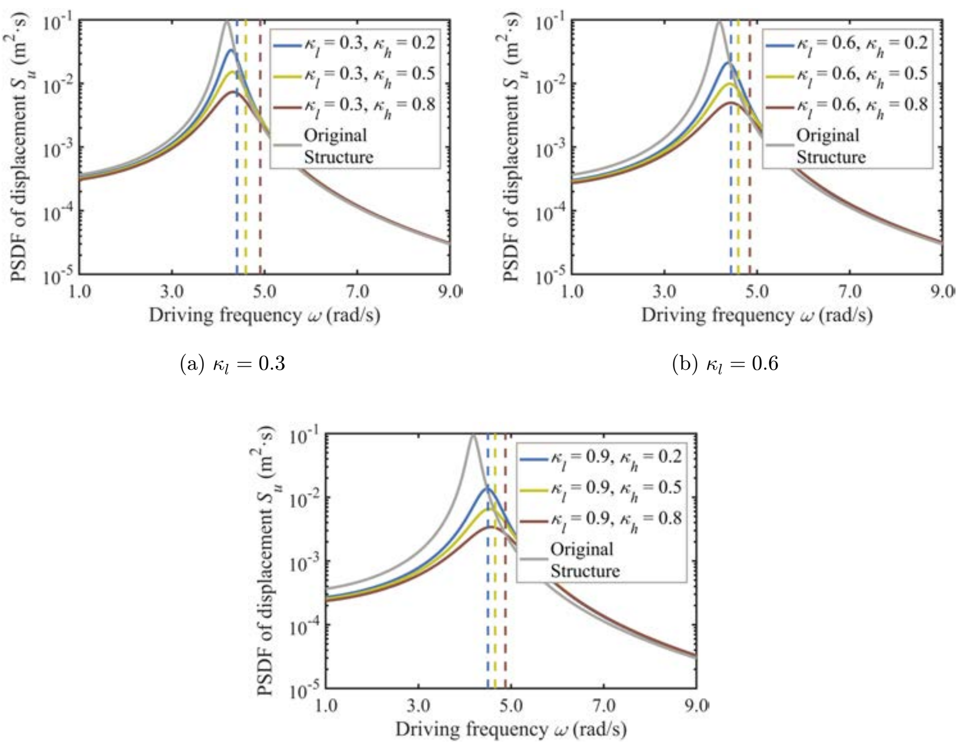

(a) $\kappa_l = 0.3$

(b) $\kappa_l = 0.6$

(c) $\kappa_l = 0.9$

Fig. 12. Displacement PSDFs of the SDOF structures with different DSD systems for $T = -10°C$, $\kappa_l \in [0.3, 0.9]$ and $\kappa_h \in [0.2, 0.8]$.

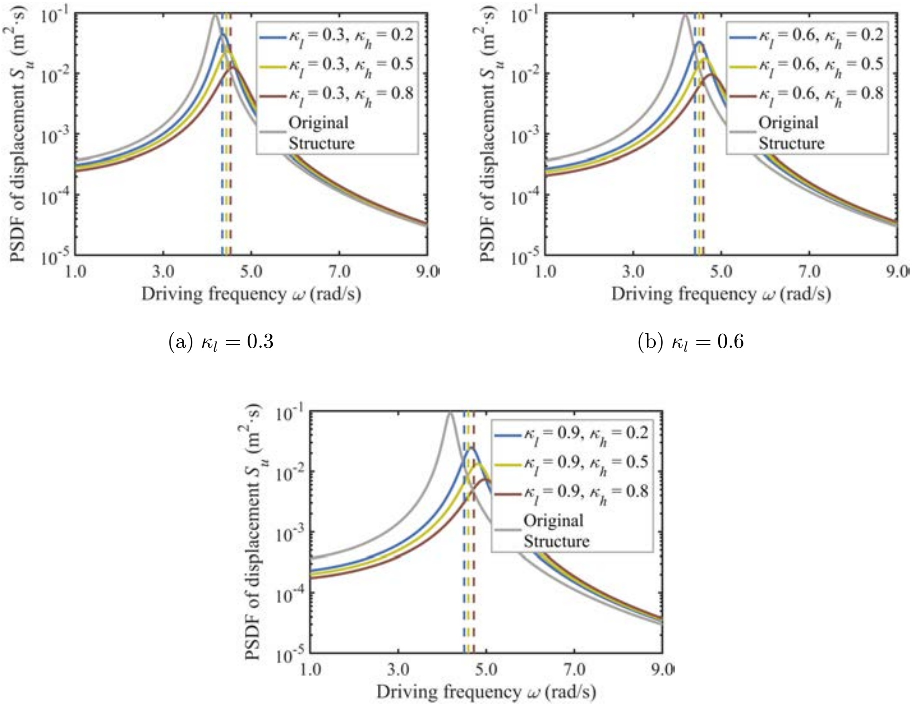

(a) $\kappa_l = 0.3$

(b) $\kappa_l = 0.6$

(c) $\kappa_l = 0.9$

Fig. 13. Displacement PSDFs of the SDOF structures with different DSD systems for $T = 15°\text{C}$, $\kappa_l \in [0.3, 0.9]$ and $\kappa_h \in [0.2, 0.8]$.

The following conclusions can be drawn from Figs. 12–14 and Table 5: (1) The peak of the curve moves down to the right with increasing κ_h and κ_l, representing greater efficient bandwidth w. (2) The peak of the curve moves up with the increasing temperature T, indicating the damping effect will be weakened when the

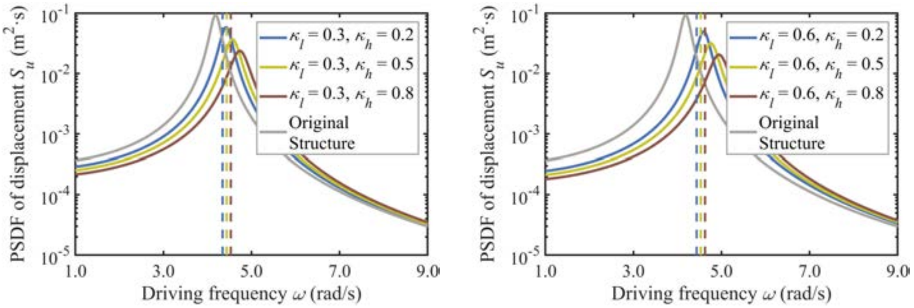

(a) $\kappa_l = 0.3$

(b) $\kappa_l = 0.6$

Fig. 14. Displacement PSDFs of the SDOF structures with different DSD systems for $T = 40°\text{C}$, $\kappa_l \in [0.3, 0.9]$ and $\kappa_h \in [0.2, 0.8]$.

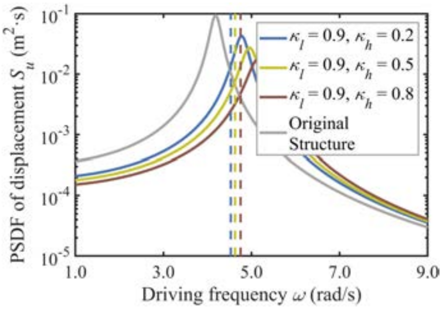

(c) $\kappa_l = 0.9$

Fig. 14. (*Continued*)

Table 5. Efficient bandwidth w (in rad/s) for different DSDs under varying temperatures.

	$T = -10°$C			$T = 15°$C			$T = 40°$C		
κ_l	$\kappa_h = 0.2$	$\kappa_h = 0.5$	$\kappa_h = 0.8$	$\kappa_h = 0.2$	$\kappa_h = 0.5$	$\kappa_h = 0.8$	$\kappa_h = 0.2$	$\kappa_h = 0.5$	$\kappa_h = 0.8$
0.3	4.404	4.593	4.907	4.342	4.436	4.530	4.342	4.436	4.530
0.6	4.436	4.593	4.844	4.404	4.499	4.593	4.436	4.530	4.624
0.9	4.499	4.656	4.876	4.499	4.593	4.719	4.530	4.624	4.750

temperature rises, and this conclusion is consistent with the previous analyses. (3) The peak also moves right with the increasing temperature T, and the efficient bandwidth w is always negatively correlated with the temperature T when the value κ_l is lower, while it decreases first and then increases with the increasing temperature T when κ_l is greater.

5. Evaluation of DSD's Performance

5.1. *Frequency-domain analysis*

To illustrate the temperature robustness on the damping effect of DSD, frequency-domain analysis for the DSD-fitted structure is implemented, which is also compared with the original structure and the structure with the conventional SMA damper. Based on the above-mentioned observations, two arbitrarily selected values $\kappa_l = 0.6$ and $\kappa_h = 0.5$ can be employed to conduct the analysis. RMS displacement ratios $\bar{\sigma}_x$ under varying temperatures ranging from $-10°$C to $40°$C are shown in Fig. 15(a). It can be observed that the RMS displacement ratios $\bar{\sigma}_x$ of the structure with the conventional SMA damper increase when the temperature T increases, which once again implies its poor temperature robustness. On the contrary, the performance degradation of DSD is delayed owing to the existence of H-SMA. In addition, a significant turning point appears around 14°C due to the completion of the inverse martensitic transformation of H-SMA, and thereon the damping effect compensation is realized.

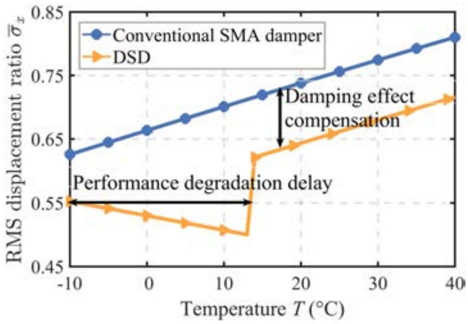

(a) RMS displacement ratios

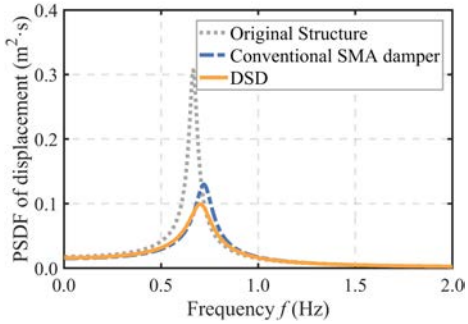

(b) Displacement PSDFs at −10°C

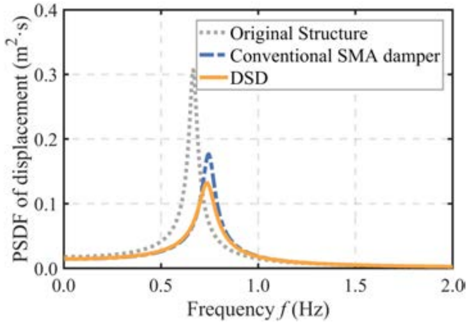

(c) Displacement PSDFs at 15°C

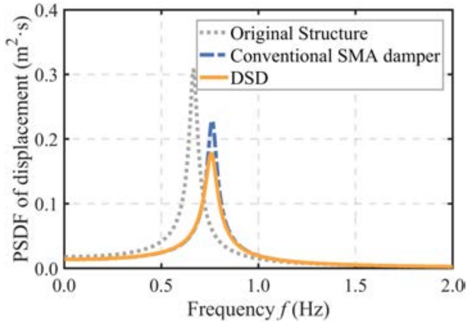

(d) Displacement PSDFs at 40°C

Fig. 15. RMS displacement ratios and displacement PSDFs under varying temperatures.

Displacement PSDFs are also given in Figs. 15(b)–15(d). It can be observed that both the peaks of the curves of the structures with DSD and with the conventional SMA damper move up to right with the increasing temperature, whereas the PSDF curve of the structure with DSD is always below that of the structure with the conventional SMA damper, and the former's efficient bandwidth is no less than the conventional one. Therefore, the temperature robustness on structural response mitigation of DSD is better than that of the conventional one.

As shown in Fig. 16, the relationship between DSD's residual deformation u_{res} and environmental temperature T is given. It can be seen that the residual deformation decreases with the temperature increasing, and the residual deformation is negligible when the temperature exceeds 14°C, since the H-SMA element has been transformed from martensite to austenite at that time.

5.2. *Time-domain analysis*

To further validate the result derived in the frequency-domain analysis, three recorded and one artificial[70,71] ground motions with PGA $= 0.5\,$g[11] are employed for the time-domain analysis. These ground motions are recorded by different stations

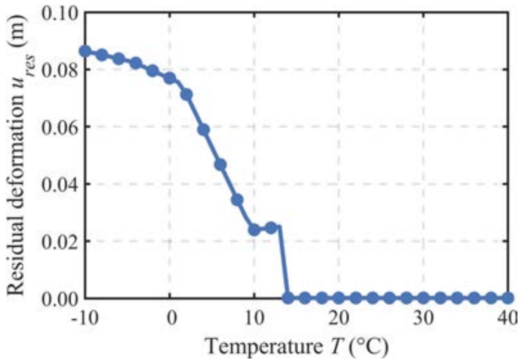

Fig. 16. Residual deformation under varying temperatures.

and composed of different frequency components, representing the diversity of geographical conditions. The acceleration response spectra of the four ground motions are shown in Fig. 17. The details of the seismic excitation are shown in Table 6.

Under the excitation of these ground motions, the displacement time histories of the original structure, as well as the structures with the conventional SMA damper and DSD under three typical temperatures (−10°C, 15°C, and 40°C) are shown in Figs. 18–21.

According to Figs. 18–21, RMS and peak structural displacement response mitigation ratios can be obtained and shown in Table 7. The results show that DSD

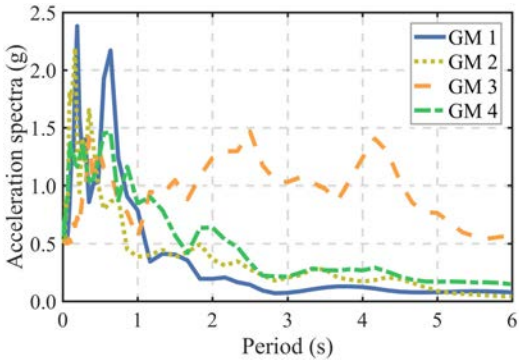

Fig. 17. Acceleration spectra of input ground accelerations.

Table 6. Detailed information of the selected ground motions.

ID #	Earthquake	Date	Station
GM 1	Southern Calif	11/22/1952	San Luis Obispo
GM 2	Superstition Hills-01	11/24/1987	Imperial Valley Wildlife Liquefaction Array
GM 3	Chi-Chi Taiwan	9/20/1999	TCU115
GM 4	Artificial excitation[70,71]	—	—

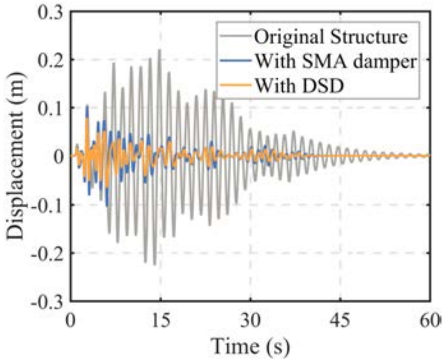

(a) $T = -10°\mathrm{C}$

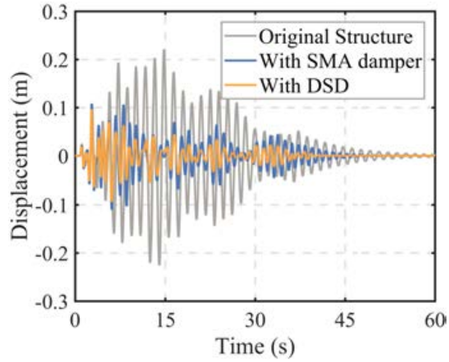

(b) $T = 15°\mathrm{C}$

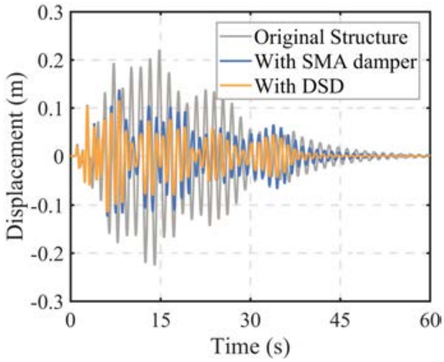

(c) $T = 40°\mathrm{C}$

Fig. 18. Time histories of structural displacements under varying temperatures and GM 1: Southern Calif.

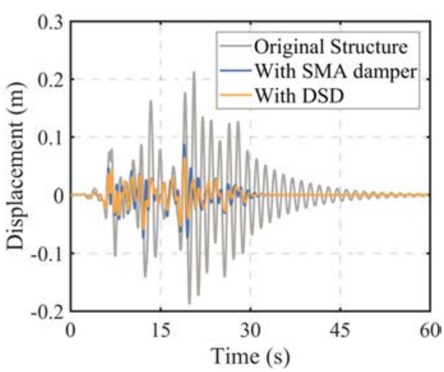

(a) $T = -10°\mathrm{C}$

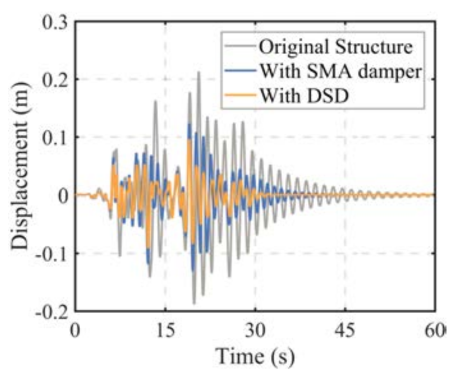

(b) $T = 15°\mathrm{C}$

Fig. 19. Time histories of structural displacements under varying temperatures and GM 2: Superstition Hills-01.

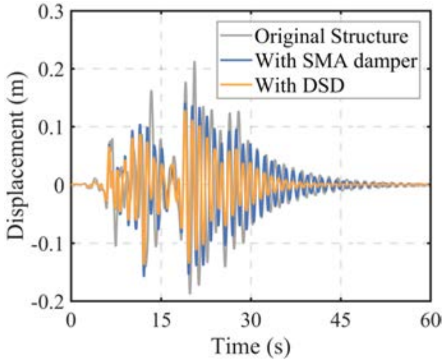

(c) $T = 40^{\circ}$C

Fig. 19. (*Continued*)

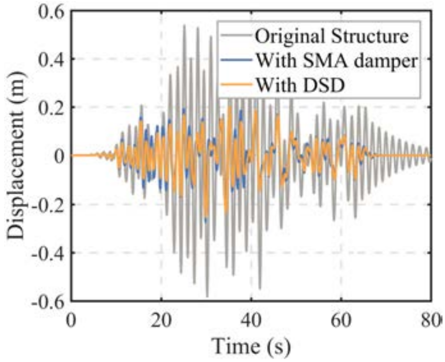

(a) $T = -10^{\circ}$C

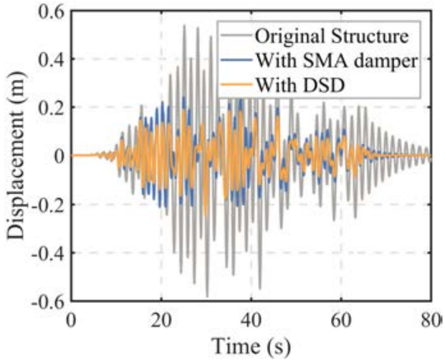

(b) $T = 15^{\circ}$C

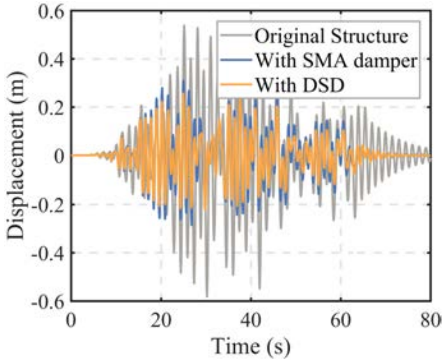

(c) $T = 40^{\circ}$C

Fig. 20. Time histories of structural displacements under varying temperatures and GM 3: Chi-Chi Taiwan.

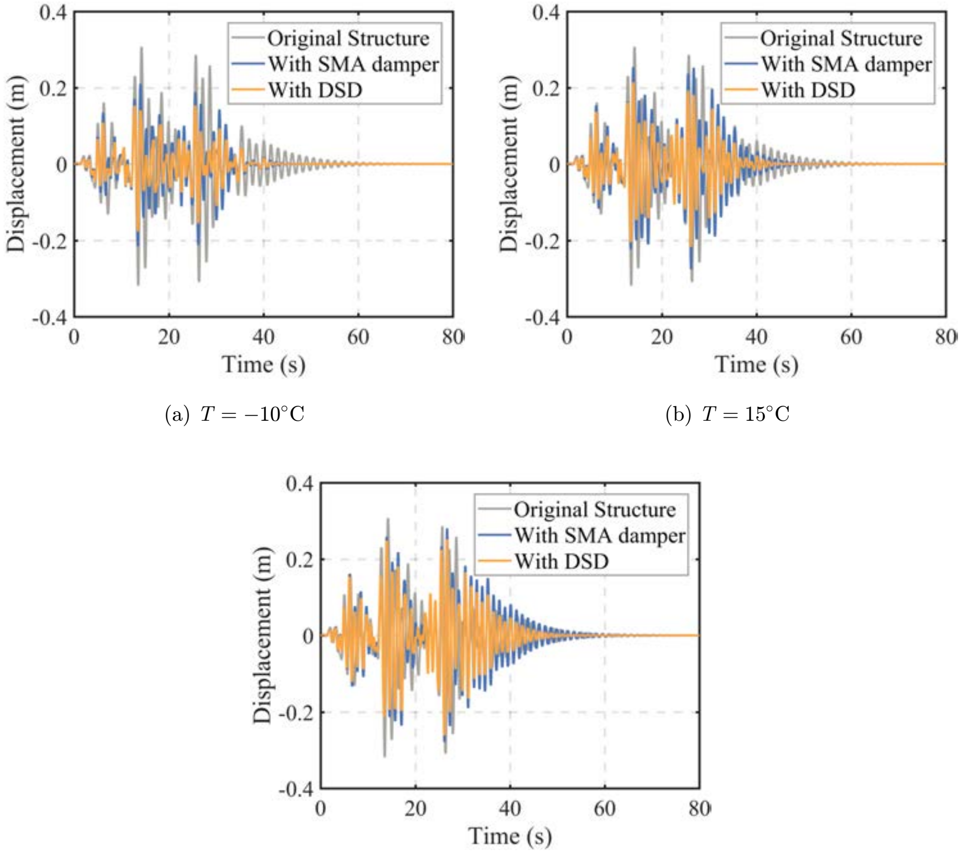

(a) $T = -10°\mathrm{C}$

(b) $T = 15°\mathrm{C}$

(c) $T = 40°\mathrm{C}$

Fig. 21. Time histories of structural displacements under varying temperatures and GM 4: Artificial excitation.

reduces the structural displacement more than the conventional SMA damper under any given temperatures and ground motions. It is evident that the average improvements of 23.4% on the RMS response mitigation ratio and 16.0% on the peak response mitigation ratio are realized. These improvements imply DSD has better temperature robustness on structural response mitigation than the conventional one.

As a further illustration, the normalized energy–time curves of SDOF structures incorporated with different control systems under the recorded ground motion GM3 and the temperature $T = 40°\mathrm{C}$ are shown in Fig. 22. It can be observed that the capacity of seismic energy dissipation of DSD is more satisfactory than the conventional SMA damper.

To better verify the effectiveness of DSD's working principle, force–deformation curves of DSD and the conventional SMA damper under GM3 are shown in Fig. 23,

Table 7. RMS and peak response mitigation ratios of the conventional SMA damper and DSD.

		RMS response mitigation ratio			Peak response mitigation ratio		
Temperature	GM	Conventional SMA damper	DSD	Improvement (%)	Conventional SMA damper	DSD	Improvement (%)
$T = -10°C$	GM 1	0.261	0.182	30.2	0.460	0.349	24.0
	GM 2	0.287	0.236	17.9	0.411	0.303	26.2
	GM 3	0.360	0.346	3.8	0.468	0.434	7.3
	GM 4	0.656	0.475	27.6	0.674	0.554	17.8
$T = 15°C$	GM 1	0.392	0.255	34.9	0.490	0.427	12.7
	GM 2	0.536	0.344	35.8	0.614	0.451	26.6
	GM 3	0.429	0.338	21.2	0.436	0.426	2.3
	GM 4	0.894	0.655	25.6	0.865	0.682	21.2
$T = 40°C$	GM 1	0.548	0.409	25.4	0.613	0.512	16.4
	GM 2	0.804	0.603	25.0	0.743	0.645	13.2
	GM 3	0.526	0.428	18.7	0.532	0.441	17.2
	GM 4	0.987	0.848	14.1	0.880	0.821	6.8
Average	—	—	—	23.4	—	—	16.0

and the exact force–deformation behaviors of two SMA elements in DSD are also given in Fig. 24. When the temperature is $-10°C$, L-SMA is transformed into austenite and H-SMA is in martensite (Fig. 24(a)). Hence, the robust self-centering ability provided by L-SMA and the adequate energy dissipation capacity supplied by H-SMA are both realized (Fig. 23(a)). As the temperature rises to $15°C$, H-SMA transforms from martensite to austenite (Fig. 24(b)), the sum of areas of hysteresis loops of austenite L-SMA and H-SMA elements reaches the maximum, resulting in a significant energy dissipation effect (Fig. 23(b)). When the temperature rises to $40°C$, the area of the hysteresis loop of L-SMA decreases gradually, whereas H-SMA can still supply the additional energy dissipation capacity, which is therefore still at a sufficient level (Fig. 24(c)). Thus, the temperature robustness of DSD is realized by the combination of L-SMA and H-SMA (Fig. 23(c)).

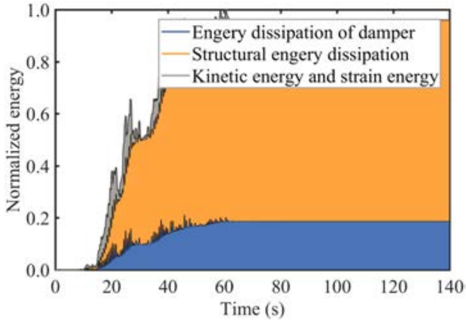

(a) With the conventional SMA damper

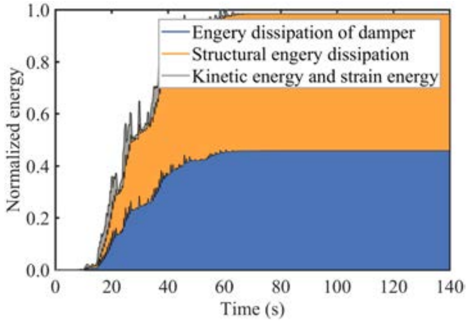

(b) With DSD

Fig. 22. Normalized energy–time curves of SDOF structures installed with different control systems.

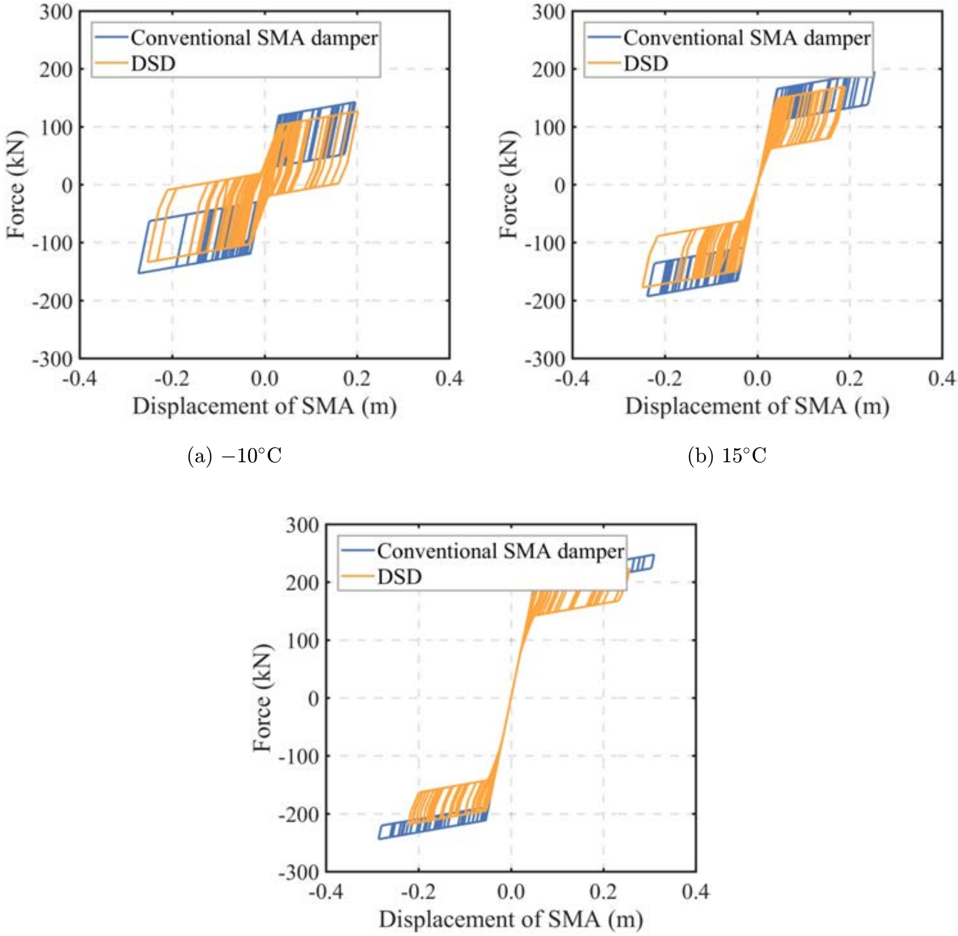

(a) -10°C

(b) 15°C

(c) 40°C

Fig. 23. Force–deformation curves of DSD and the conventional SMA damper under (a) -10°C, (b) 15°C, and (c) 40°C, and the recorded ground motion GM3.

6. Application of DSD in MDOF Structures

6.1. *Motion-governing equations*

In the previous sections, the effectiveness of DSD installed in SDOF structures has been verified. To illustrate the extensibility of the proposed DSD for MDOF structures, further numerical analysis is given in this section. As shown in Fig. 25, the analytical model of an MDOF structure with DSD systems is employed to investigate DSD's performance, and the corresponding equivalent model is given in Fig. 26. In these figures, m_i, c_i, and k_i are the mass, damping, and stiffness coefficients of the ith floor of the primary structure. $k_{h,i}$ and $k_{l,i}$ are the initial stiffness coefficients of

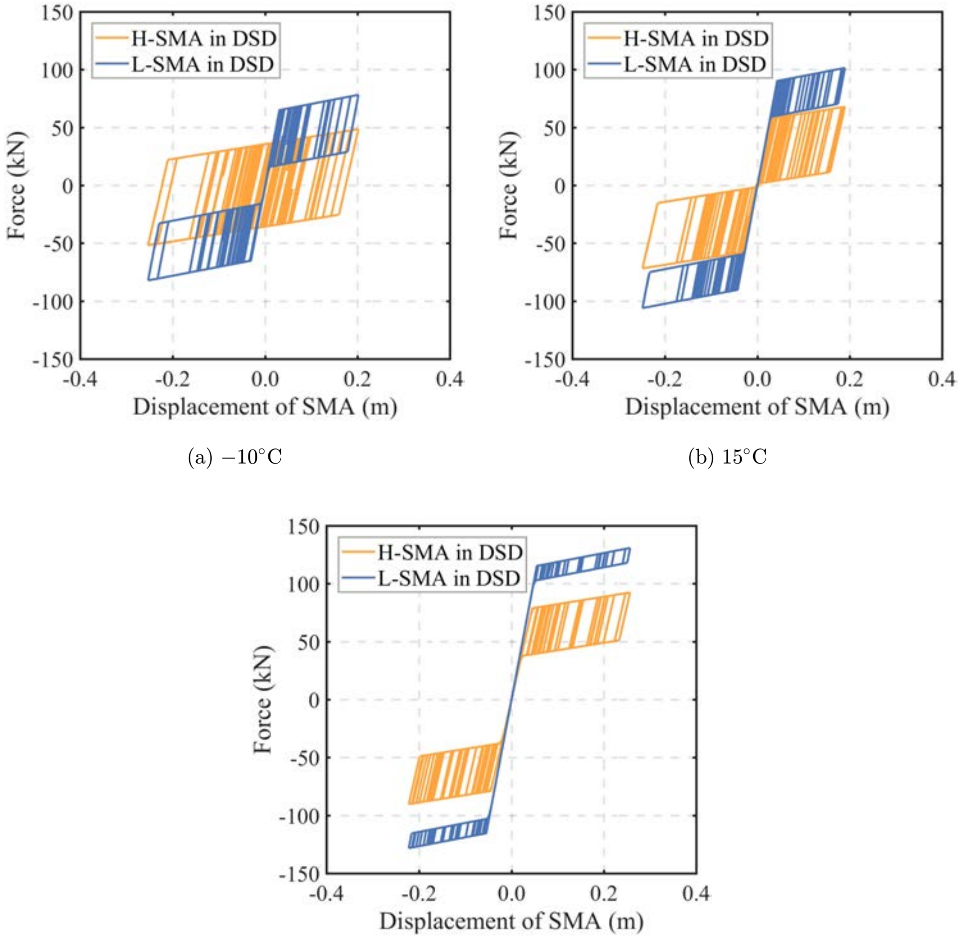

(a) $-10°$C

(b) $15°$C

(c) $40°$C

Fig. 24. Force–deformation curves of SMA elements in DSD under (a) $-10°$C, (b) $15°$C, and (c) $40°$C, and the recorded ground motion GM3.

H-SMA and L-SMA elements, respectively. $\tilde{k}_{eh,i}$, $\tilde{c}_{eh,i}$, $\tilde{k}_{el,i}$, and $\tilde{c}_{el,i}$ are the equivalent parameters of SMA elements in DSD systems.

The motion-governing equation for the MDOF structure assisted by DSD systems subjected to the ground motion can be written as

$$m_i\ddot{x}_i + c_i(\dot{x}_i - \dot{x}_{i-1}) + k_i(x_i - x_{i-1}) + F_{s,i}(x_i, x_{i-1}, \dot{x}_i, \dot{x}_{i-1}) = -m_i\ddot{x}_g, \tag{30}$$

where $\ddot{x}_i$ is the displacement of the ith floor of the primary structure with respect to the ground. The respective velocity and acceleration are denoted as $\dot{x}_i$ and $\ddot{x}_i$. The overall output force $F_{s,i}$ of DSD in the ith floor can be expressed as

$$F_{s,i}(x_i, x_{i-1}, \dot{x}_i, \dot{x}_{i-1}) = (\tilde{c}_{el,i} + \tilde{c}_{eh,i})(\dot{x}_i - \dot{x}_{i-1}) + (\tilde{k}_{el,i} + \tilde{k}_{eh,i})(x_i - x_{i-1}), \tag{31}$$

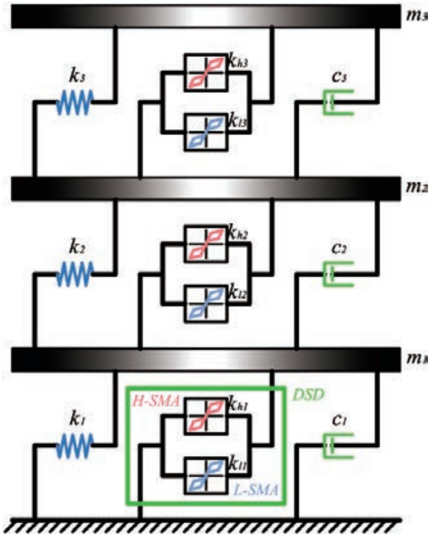

Fig. 25. Analytical model of the MDOF structure with DSD systems.

where the equivalent parameters of DSD are given as

$$\begin{aligned}\tilde{k}_{e,i} &= \alpha_{d,i}k_{d,i} + (1-\alpha_{d,i})k_{d,i}\frac{u_{b,i}+u_{a,i}}{\sqrt{2\pi}\sigma_{\delta_i}}e^{-\frac{u_{a,i}^2}{2\sigma_{\delta_i}^2}},\\ \tilde{c}_{e,i} &= (1-\alpha_{d,i})k_{d,i}\frac{u_{b,i}-u_{a,i}}{\sqrt{2\pi}\sigma_{\dot{\delta}_i}}\left[1-\mathrm{erf}\left(\frac{u_{a,i}}{\sqrt{2}\sigma_{\delta_i}}\right)\right],\end{aligned} \tag{32}$$

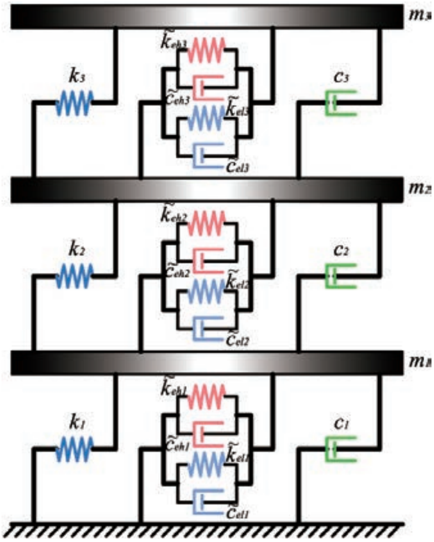

Fig. 26. Equivalent model of MDOF structure with DSD systems.

or

$$\tilde{k}_{e,i} = \alpha_{d,i} k_{d,i}, \quad \tilde{c}_{e,i} = (1-\alpha_{d,i}) k_{d,i} \sqrt{\frac{2}{\pi}} \frac{u_{a,i}}{\sigma_{\dot{\delta}_i}}. \tag{33}$$

In Eqs. (32) and (33), $\alpha_{d,i}$, $k_{d,i}$, $u_{a,i}$, and $u_{b,i}$ are the material properties of SMA elements of the ith floor. The variables $\delta_i = x_i - x_{i-1}$ and $\dot{\delta}_i = \dot{x}_i - \dot{x}_{i-1}$ are the inter-story displacement and velocity, respectively, and we have

$$\begin{cases} \sigma_{\delta_i}^2 = \mathrm{E}[\delta_i^2] = \mathrm{E}[(x_i - x_{i-1})^2] = \mathrm{E}[x_i^2] + \mathrm{E}[x_{i-1}^2] = \sigma_{x_i}^2 + \sigma_{x_{i-1}}^2 \\ \sigma_{\dot{\delta}_i}^2 = \mathrm{E}[\dot{\delta}_i^2] = \mathrm{E}[(\dot{x}_i - \dot{x}_{i-1})^2] = \mathrm{E}[\dot{x}_i^2] + \mathrm{E}[\dot{x}_{i-1}^2] = \sigma_{\dot{x}_i}^2 + \sigma_{\dot{x}_{i-1}}^2 \end{cases}, \tag{34}$$

where it should be noted that x_i and $\dot{x}_i$ are statistically independent and normally distributed random variables with zero means.

Substituting Eq. (31) into Eq. (30) gives

$$m_i \ddot{x}_i + (c_i + \tilde{c}_{el,i} + \tilde{c}_{eh,i})(\dot{x}_i - \dot{x}_{i-1}) + (k_i + \tilde{k}_{el,i} + \tilde{k}_{eh,i})(x_i - x_{i-1}) = -m_i \ddot{x}_g, \tag{35}$$

which can be written in the matrix form as

$$\mathbf{M}\ddot{\mathbf{x}} + (\mathbf{C} + \mathbf{C}_{el} + \mathbf{C}_{eh})\dot{\mathbf{x}} + (\mathbf{K} + \mathbf{K}_{el} + \mathbf{K}_{eh})\mathbf{x} = -\mathbf{M}\mathbf{1}\ddot{x}_g. \tag{36}$$

The matrices and vectors in Eq. (36) are given as follows:

$$\begin{gathered} \mathbf{M} = \begin{bmatrix} m_1 & & \\ & m_2 & \\ & & m_3 \end{bmatrix}, \quad \mathbf{C} = \begin{bmatrix} c_1 + c_2 & -c_2 & \\ -c_2 & c_2 + c_3 & -c_3 \\ & -c_3 & c_3 \end{bmatrix}, \\ \mathbf{K} = \begin{bmatrix} k_1 + k_2 & -k_2 & \\ -k_2 & k_2 + k_3 & -k_3 \\ & -k_3 & k_3 \end{bmatrix}, \end{gathered} \tag{37}$$

$$\begin{gathered} \mathbf{C}_{el} = \begin{bmatrix} \tilde{c}_{el,1} + \tilde{c}_{el,2} & -\tilde{c}_{el,2} & \\ -\tilde{c}_{el,2} & \tilde{c}_{el,2} + \tilde{c}_{el,3} & -\tilde{c}_{el,3} \\ & -\tilde{c}_{el,3} & \tilde{c}_{el,3} \end{bmatrix}, \\ \mathbf{C}_{eh} = \begin{bmatrix} \tilde{c}_{eh,1} + \tilde{c}_{eh,2} & -\tilde{c}_{eh,2} & \\ -\tilde{c}_{eh,2} & \tilde{c}_{eh,2} + \tilde{c}_{eh,3} & -\tilde{c}_{eh,3} \\ & -\tilde{c}_{eh,3} & \tilde{c}_{eh,3} \end{bmatrix}, \end{gathered} \tag{38}$$

$$\begin{gathered} \mathbf{K}_{el} = \begin{bmatrix} \tilde{k}_{el,1} + \tilde{k}_{el,2} & -\tilde{k}_{el,2} & \\ -\tilde{k}_{el,2} & \tilde{k}_{el,2} + \tilde{k}_{el,3} & -\tilde{k}_{el,3} \\ & -\tilde{k}_{el,3} & \tilde{k}_{el,3} \end{bmatrix}, \\ \mathbf{K}_{eh} = \begin{bmatrix} \tilde{k}_{eh,1} + \tilde{k}_{eh,2} & -\tilde{k}_{eh,2} & \\ -\tilde{k}_{eh,2} & \tilde{k}_{eh,2} + \tilde{k}_{eh,3} & -\tilde{k}_{eh,3} \\ & -\tilde{k}_{eh,3} & \tilde{k}_{eh,3} \end{bmatrix}, \end{gathered} \tag{39}$$

$$\ddot{\mathbf{x}} = \begin{Bmatrix} \ddot{x}_1 \\ \ddot{x}_2 \\ \ddot{x}_3 \end{Bmatrix}, \quad \dot{\mathbf{x}} = \begin{Bmatrix} \dot{x}_1 \\ \dot{x}_2 \\ \dot{x}_3 \end{Bmatrix}, \quad \mathbf{x} = \begin{Bmatrix} x_1 \\ x_2 \\ x_3 \end{Bmatrix}, \quad \mathbf{1} = \begin{Bmatrix} 1 \\ 1 \\ 1 \end{Bmatrix}. \tag{40}$$

Combined with the Kanai–Tajimi stochastic model[68] shown in Eq. (18), the state vector of the structure–DSD system can be defined as

$$\mathbf{u} = \{\mathbf{x}, x_f, \dot{\mathbf{x}}, \dot{x}_f\}^{\mathrm{T}}. \tag{41}$$

Then the motion-governing equation given in Eq. (36) can be written in the state space form as

$$\frac{\mathrm{d}\mathbf{u}}{\mathrm{d}t} = \mathbf{A}\mathbf{u} + \mathbf{w}, \tag{42}$$

where $\mathbf{w} = \{\mathbf{0}_{1\times 7} \ \ -\ddot{w}\}^{\mathrm{T}}$ is a column vector that contains the intensity of the white noise, and $\mathbf{A}$ is an augmented matrix expressed as

$$\mathbf{A} = \begin{bmatrix} \mathbf{O}_{3\times 3} & \mathbf{0}_{3\times 1} & \mathbf{I}_{3\times 3} & \mathbf{0}_{3\times 1} \\ \mathbf{0}_{1\times 3} & 0 & \mathbf{0}_{1\times 3} & 1 \\ -\mathbf{M}^{-1}(\mathbf{K} + \mathbf{K}_{el} + \mathbf{K}_{eh}) & \omega_f^2 \mathbf{1}_{3\times 1} & -\mathbf{M}^{-1}(\mathbf{C} + \mathbf{C}_{el} + \mathbf{C}_{eh}) & 2\xi_f \omega_f \mathbf{1}_{3\times 1} \\ \mathbf{0}_{1\times 3} & -\omega_f^2 & \mathbf{0}_{1\times 3} & -2\xi_f \omega_f \end{bmatrix}_{8\times 8}, \tag{43}$$

where $\mathbf{O}_{3\times 3}$ is the zero matrix, $\mathbf{0}_{3\times 1}$ the zero column vector, $\mathbf{0}_{1\times 3}$ the zero row vector, and $\mathbf{I}_{3\times 3}$ the identity matrix. Assuming that the responses are stationary and Markovian, then the evolution equation can be obtained as[62]

$$\frac{\mathrm{d}\mathbf{C}_{uu}}{\mathrm{d}t} = \mathbf{A}\mathbf{C}_{uu} + \mathbf{C}_{uu}\mathbf{A}^{\mathrm{T}} + \mathbf{S}_{ww} = 0, \tag{44}$$

where $\mathbf{S}_{ww} = \mathrm{diag}\{\mathbf{0}_{1\times 7}, 2\pi S_0\}$ is the diagonal input matrix of the excitation of rock bed, and $\mathbf{C}_{uu}$ is the covariance matrix of the state vector $\mathbf{u}$, which could be written as

$$\mathbf{C}_{uu} = \begin{bmatrix} \sigma_{x_1}^2 & \sigma_{x_1 x_2} & \sigma_{x_1 x_3} & \sigma_{x_1 x_f} & \sigma_{x_1 \dot{x}_1} & \sigma_{x_1 \dot{x}_2} & \sigma_{x_1 \dot{x}_3} & \sigma_{x_1 \dot{x}_f} \\ & \sigma_{x_2}^2 & \sigma_{x_2 x_3} & \sigma_{x_2 x_f} & \sigma_{x_2 \dot{x}_1} & \sigma_{x_2 \dot{x}_2} & \sigma_{x_2 \dot{x}_3} & \sigma_{x_2 \dot{x}_f} \\ & & \sigma_{x_3}^2 & \sigma_{x_3 x_f} & \sigma_{x_3 \dot{x}_1} & \sigma_{x_3 \dot{x}_2} & \sigma_{x_3 \dot{x}_3} & \sigma_{x_3 \dot{x}_f} \\ & & & \sigma_{x_f}^2 & \sigma_{x_f \dot{x}_1} & \sigma_{x_f \dot{x}_2} & \sigma_{x_f \dot{x}_3} & \sigma_{x_f \dot{x}_f} \\ & & & & \sigma_{\dot{x}_1}^2 & \sigma_{\dot{x}_1 \dot{x}_2} & \sigma_{\dot{x}_1 \dot{x}_3} & \sigma_{\dot{x}_1 \dot{x}_f} \\ & & & & & \sigma_{\dot{x}_2}^2 & \sigma_{\dot{x}_2 \dot{x}_3} & \sigma_{\dot{x}_2 \dot{x}_f} \\ & & & & & & \sigma_{\dot{x}_3}^2 & \sigma_{\dot{x}_3 \dot{x}_f} \\ \text{sym.} & & & & & & & \sigma_{\dot{x}_f}^2 \end{bmatrix}. \tag{45}$$

Finally, the structural and the DSD's responses can be solved by several iterations until the convergence of $\mathbf{C}_{uu}$.

Table 8. Default values of parameters of the MDOF structure.

Floor number i	1	2	3
Story mass m_i (kg)	98.3	98.3	98.3
Story stiffness k_i (N/m)	5160	6840	6840
Story damping c_i ($\mathrm{N \cdot s/m}$)	125	50	50

6.2. *Frequency-domain analysis*

For the frequency-domain analysis of MDOF structure with DSD systems, a 3-story benchmark model[12] is used as a representative example and the corresponding parameters are given in Table 8. In this 3-story model, the story stiffness coefficients are taken as 1/100 of the original values such that uncontrolled structural responses have the same order as the SDOF structure in the previous sections. In addition, SMA parameters in all the floors are set to be the same values as the previous examples. It should be noted that one could obtain the optimal design parameters of DSD with numerical schemes such as the genetic algorithm, which is out of the scope of current work.

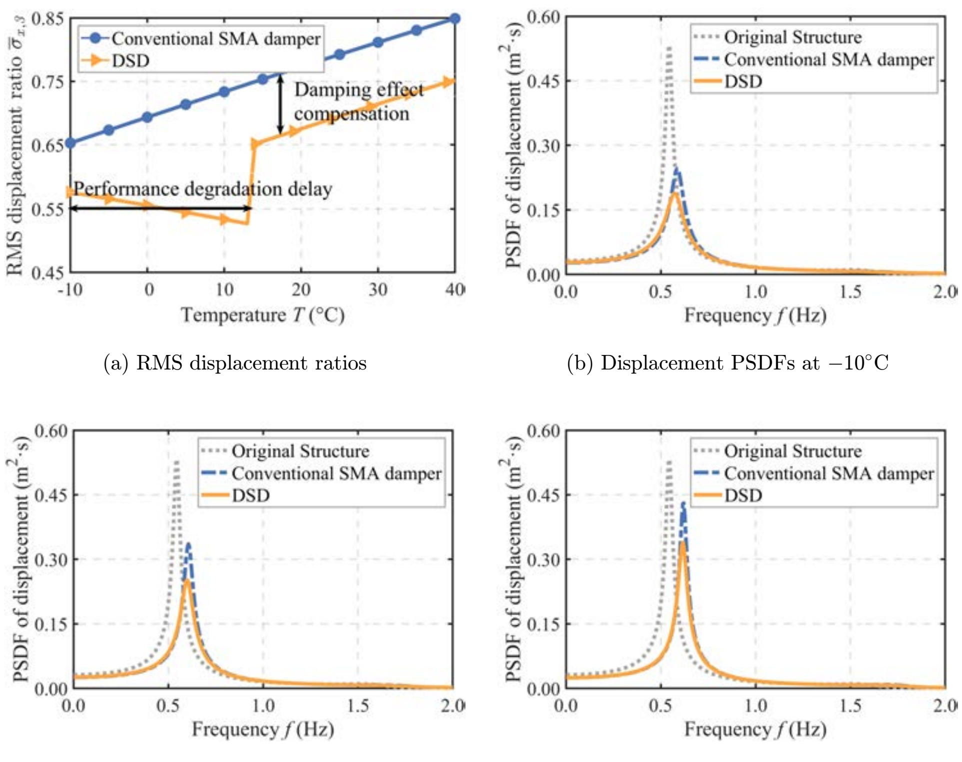

(a) RMS displacement ratios

(b) Displacement PSDFs at −10°C

(c) Displacement PSDFs at 15°C

(d) Displacement PSDFs at 40°C

Fig. 27. RMS displacement ratios and displacement PSDFs under varying temperatures.

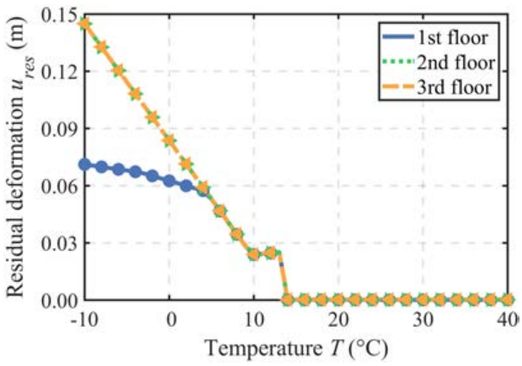

Fig. 28. Residual deformation under varying temperatures.

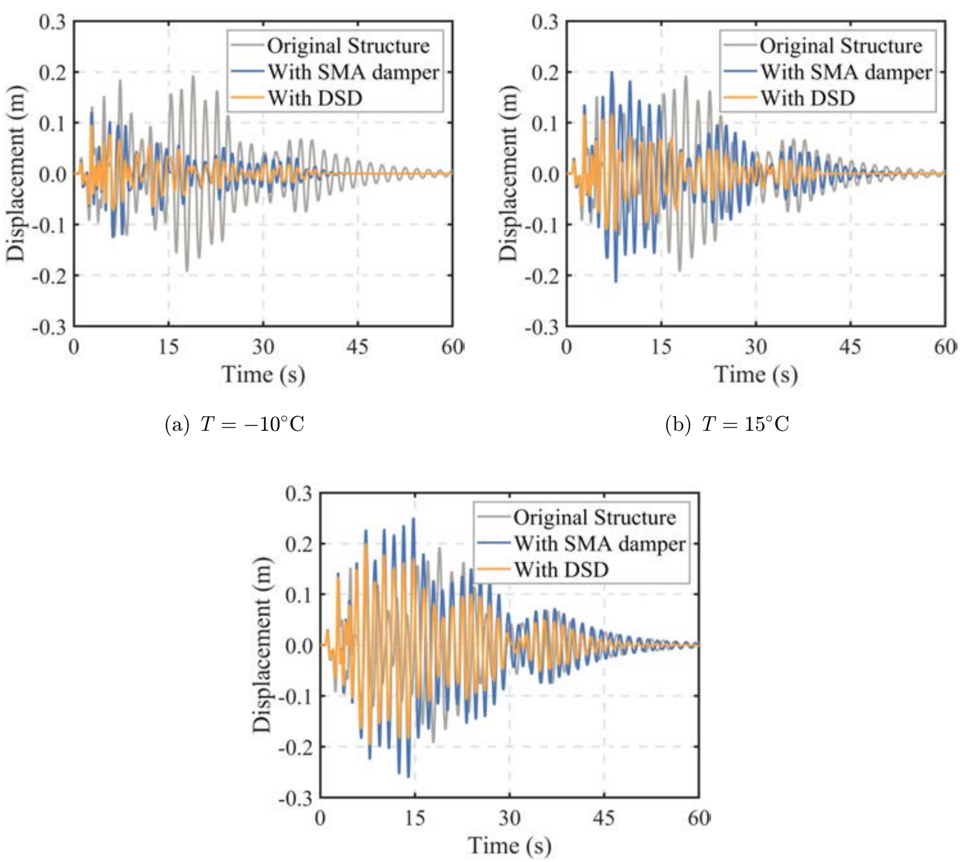

(a) $T = -10^{\circ}$C

(b) $T = 15^{\circ}$C

(c) $T = 40^{\circ}$C

Fig. 29. Time histories of structural displacements under varying temperatures and GM 1: Southern Calif.

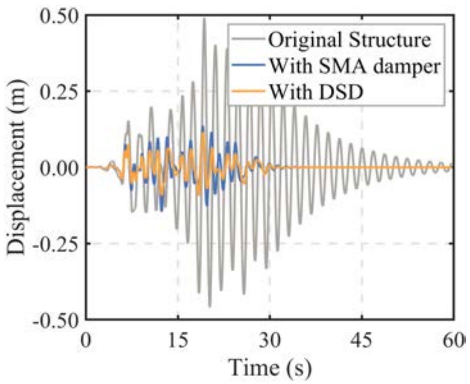

(a) $T = -10°\text{C}$

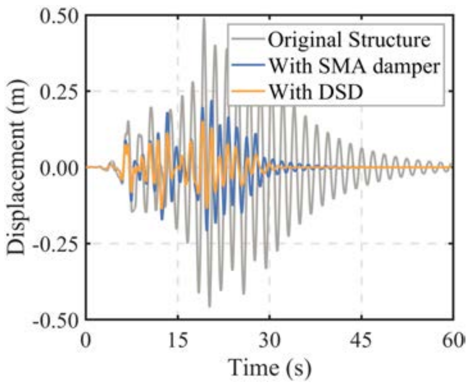

(b) $T = 15°\text{C}$

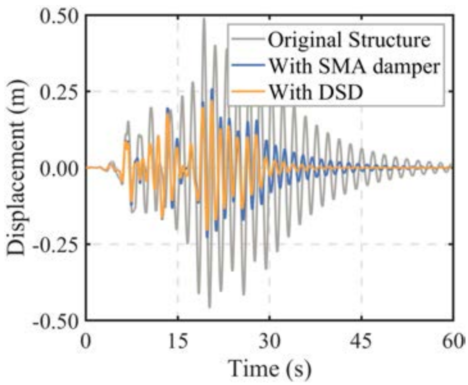

(c) $T = 40°\text{C}$

Fig. 30. Time histories of structural displacements under varying temperatures and GM 2: Superstition Hills-01.

To illustrate the temperature robustness on the damping effect of DSD, RMS displacement ratios of the top floor (i.e. the third floor) $\bar{\sigma}_{x,3}$ under varying temperatures ranging from $-10°\text{C}$ to $40°\text{C}$ are shown in Fig. 27(a). It can be observed that the displacement ratios $\bar{\sigma}_{x,3}$ of the structure with conventional SMA damper increase with the temperature T increasing, while the performance degradation of DSD is delayed owing to the existence of H-SMA. Moreover, a turning point appears around $14°\text{C}$ due to the completion of an inverse martensitic transformation of H-SMA, and hence the damping effect compensation is realized.

Displacement PSDFs of the third floor are also given in Figs. 27(b)–27(d). It can still be observed that both the peaks of the curves of DSD and conventional SMA damper move up to right with the temperature increasing. In addition, the PSDF curve of the DSD is always below that of the conventional SMA damper, and its efficient bandwidth is no less than the conventional one. Therefore, the temperature

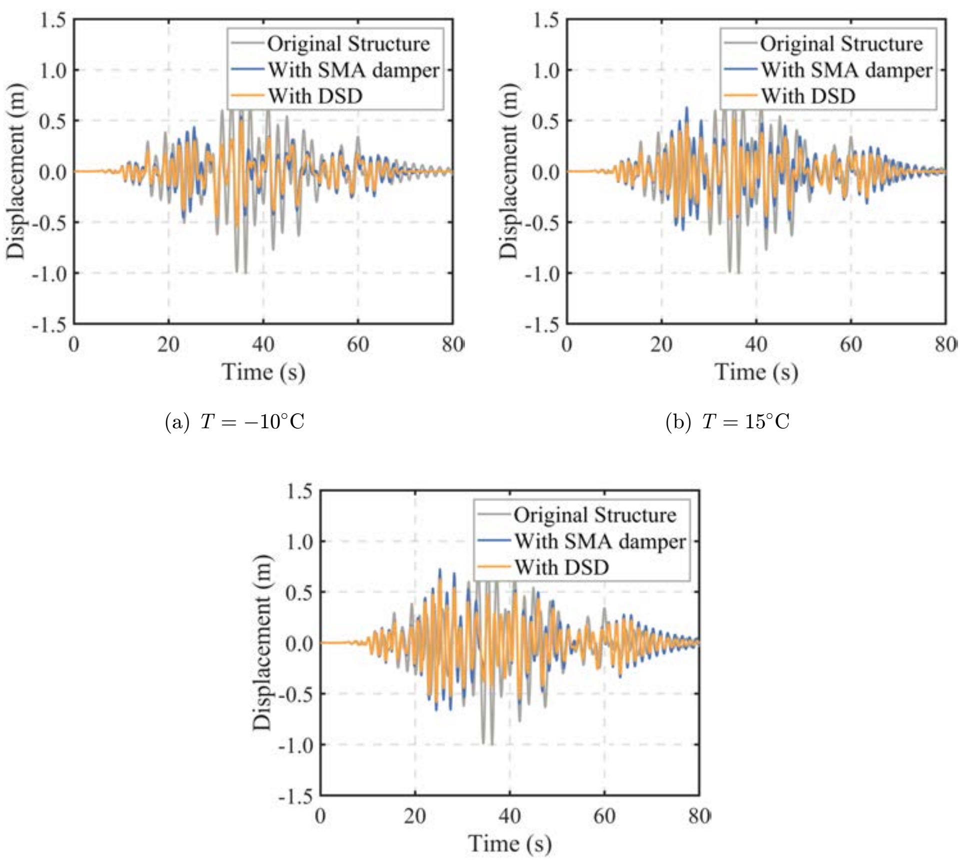

(a) $T = -10°C$ (b) $T = 15°C$ (c) $T = 40°C$

Fig. 31. Time histories of structural displacements under varying temperatures and GM 3: Chi-Chi Taiwan.

robustness on structural response mitigation of DSD can still be obtained for the MDOF structures as expected.

As shown in Fig. 28, the relationships between DSD's residual deformation u_{res} and environmental temperature T are given. It can be seen that the residual deformation of all three floors decreases with the increasing temperature, and the residual deformation is negligible when the temperature exceeds 14°C, which coincides with the conclusion obtained from the analysis for the SDOF structure.

6.3. *Time-domain analysis*

To further validate the result derived in the frequency-domain analysis, the same ground motions shown in Table 6 and Fig. 17 are employed for time-domain analysis.

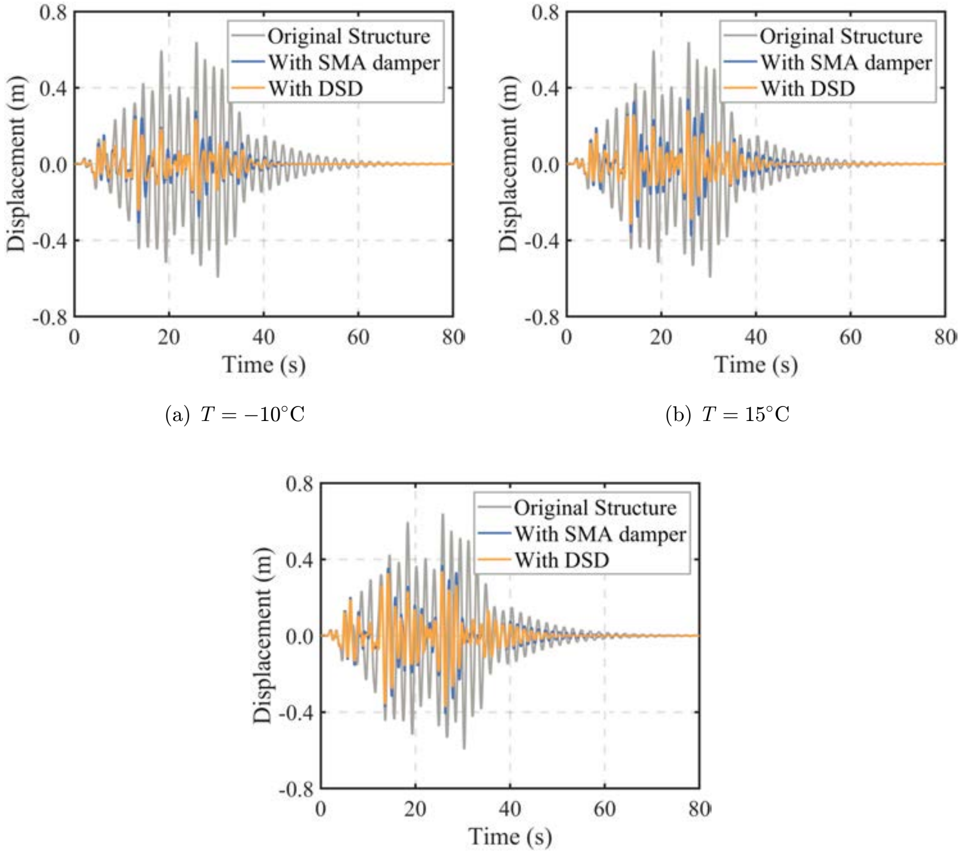

(a) $T = -10°C$ (b) $T = 15°C$ (c) $T = 40°C$

Fig. 32. Time histories of structural displacements under varying temperatures and GM 4: Artificial excitation.

Under the excitation of these ground motions, the displacement time histories of the third floor of the original structure, the structures with conventional SMA damper, and with DSD under three typical temperatures ($-10°C$, $15°C$, and $40°C$) are shown in Figs. 29–32.

According to Figs. 29–32, RMS and peak structural displacement response mitigation ratios of the third floor can be obtained and shown in Table 9. The results show that DSD reduces the structural displacement more than the conventional SMA damper in most cases. It is evident that average improvements of 23.8% on the RMS response mitigation ratio and 19.7% on the peak response mitigation ratio are realized. These improvements imply DSD still has better temperature robustness on structural response mitigation than the conventional one in MDOF structures.

Table 9. RMS and peak response mitigation ratios of the conventional SMA damper and DSD.

		RMS response mitigation ratio			Peak response mitigation ratio		
Temperature	GM	Conventional SMA damper	DSD	Improvement (%)	Conventional SMA damper	DSD	Improvement (%)
$T = -10°C$	GM 1	0.459	0.311	32.4	0.656	0.500	23.8
	GM 2	0.214	0.156	27.2	0.297	0.235	20.6
	GM 3	0.559	0.449	10.7	0.499	0.502	−0.6
	GM 4	0.328	0.268	18.3	0.485	0.382	21.2
$T = 15°C$	GM 1	0.903	0.488	46.0	1.111	0.606	45.4
	GM 2	0.366	0.224	38.9	0.450	0.311	30.9
	GM 3	0.702	0.567	19.2	0.583	0.472	19.0
	GM 4	0.431	0.338	21.7	0.590	0.496	15.8
$T = 40°C$	GM 1	1.344	0.963	28.3	1.353	1.037	23.4
	GM 2	0.425	0.348	18.0	0.529	0.453	14.5
	GM 3	0.795	0.693	12.9	0.670	0.579	13.6
	GM 4	0.482	0.427	11.4	0.641	0.583	9.0
Average	—	—	—	23.8	—	—	19.7

7. Conclusions

This study investigates the possibilities of an innovative DSD system installed in both SDOF and MDOF structures subjected to seismic excitation. In the configuration of DSD, double hysteretic SMA elements with different phase transition temperatures are arranged in parallel. The following conclusions are drawn from this work:

(1) A balance between SMA dampers' residual deformation and the energy dissipation capacity can be realized by the proposed DSD system, which can mitigate the structural seismic response more effectively than the conventional SMA damper, with an acceptable residual deformation, indicating less SMA material is required to fulfill the same structural response mitigation requirement.
(2) DSD can delay the degradation of SMA's energy dissipation capacity, and significantly suppress structural seismic response under varying temperatures. This superior temperature robustness on structural response mitigation makes DSD capable of being employed in global areas in different climates.
(3) By fully utilizing the self-centering ability of L-SMA and the sufficient energy dissipation capacity of H-SMA, DSD is a promising mechanism to mitigate structural response and can be considered as a decent technology for structural vibration control in modern society.
(4) This study is a preliminary test. Combining this study with innovative techniques to minimize the material cost will be of great significance, which needs further study. Moreover, the experimental investigation to validate the theoretical analysis is also further needed.

Acknowledgments

Financial support from the National Natural Science Foundation of China through Grant Nos. 51778497 and 51778496 is highly appreciated.

References

1. T. Igusa and K. Xu, Vibration control using multiple tuned mass dampers, *J. Sound Vibr.* **175**(4) (1994) 491–503, doi: 10.1006/jsvi.1994.1341.
2. C. Pan and R. Zhang, Design of structure with inerter system based on stochastic response mitigation ratio, *Struct. Control Health Monitor.* **25**(6) (2018) e2169, doi: 10.1002/stc.2169.
3. L. Lu, Y. F. Duan, B. F. Spencer, X. Lu and Y. Zhou, Inertial mass damper for mitigating cable vibration, *Struct. Control Health Monitor.* **24**(10) (2017) e1986, doi: 10.1002/stc.1986.
4. R. Rana and T. T. Soong, Parametric study and simplified design of tuned mass dampers, *Eng. Struct.* **20**(3) (1998) 193–204, doi: 10.1016/S0141-0296(97)00078-3.
5. H. H. Tsang, S. H. Lo, X. Xu and M. Neaz Sheikh, Seismic isolation for low-to-medium-rise buildings using granulated rubber–soil mixtures: numerical study, *Earthq. Eng. Struct. Dyn.* **41**(14) (2012) 2009–2024, doi: 10.1002/eqe.2171.
6. J. Tan, P. Zhang, Q. Feng and G. Song, Passive seismic protection of building piping system: A review, *Int. J. Struct. Stab. Dyn.* **20**(3) (2020) 2030001, doi: 10.1142/S0219455420300013.
7. C. J. Jiang, Z. D. Lu and L. Z. Li, Shear performance of fire-damaged reinforced concrete beams repaired by a bolted side-plating technique, *J. Struct. Eng.* **143**(5) (2017) 04017007, doi: 10.1061/(ASCE)ST.1943-541X.0001726.
8. J. G. Teng, S. T. Smith, J. Yao and J. F. Chen, Intermediate crack-induced debonding in RC beams and slabs. *Construct. Build. Mater.* **17**(6–7) (2003) 447–462, doi: 10.1016/S0950-0618(03)00043-6.
9. R. K. L. Su, L. Z. Li and S. H. Lo, Longitudinal partial interaction in bolted side-plated reinforced concrete beams, *Adv. Struct. Eng.* **17**(7) (2014) 921–936, doi: 10.1260/1369-4332.17.7.921.
10. J. Zhou and L. Wang, Repair of fire-damaged reinforced concrete members with axial load: a review, *Sustainability* **11**(4) (2019) 963, doi: 10.3390/su11040963.
11. R. Zhang, C. Wang, C. Pan, H. Shen, Q. Ge and L. Zhang, Simplified design of elasto-plastic structures with metallic yielding dampers based on the concept of uniform damping ratio, *Eng. Struct.* **176** (2018) 734–745, doi: 10.1016/j.engstruct.2018.09.009.
12. T. Asai, Y. Araki and K. Ikago, Structural control with tuned inertial mass electromagnetic transducers, *Struct. Control Health Monitor.* **25**(2) (2018) e2059, doi: 10.1002/stc.2059.
13. A. Gonzalez-Buelga, L. R. Clare, S. A. Neild, J. Z. Jiang and D. J. Inman, An electromagnetic inerter-based vibration suppression device, *Smart Mater. Struct.* **24**(5) (2015) 055015, doi: 10.1088/0964-1726/24/5/055015.
14. K. Ikago, K. Saito and N. Inoue, Seismic control of single-degree-of-freedom structure using tuned viscous mass damper, *Earthq. Eng. Struct. Dyn.* **41**(3) (2012) 453–474, doi: 10.1002/eqe.1138.
15. K. Ikago, Y. Sugimura, K. Saito and N. Inoue, Modal response characteristics of a multiple-degree-of-freedom structure incorporated with tuned viscous mass dampers, *J. Asian Architect. Build. Eng.* **11**(2) (2012) 375–382, doi: 10.3130/jaabe.11.375.

16. D. Altieri, E. Tubaldi, M. De Angelis, E. Patelli and A. Dall'Asta, Reliability-based optimal design of nonlinear viscous dampers for the seismic protection of structural systems, *Bull. Earthq. Eng.* **16**(2) (2018) 963–982, doi: 10.1007/s10518-017-0233-4.
17. M. Gutierrez Soto and H. Adeli, Tuned mass dampers, *Arch. Comput. Methods Eng.* **20**(4) (2013) 419–431, doi: 10.1007/s11831-013-9091-7.
18. A. Oveisi, M. Hosseini-Pishrobat, T. Nestorović and J. Keighobadi, Observer-based repetitive model predictive control in active vibration suppression. *Struct. Control Health Monitor.* **25**(5) (2018) e2149, doi: 10.1002/stc.2149.
19. F. Oliveira, M. A. Botto, P. Morais and A. Suleman, Semi-active structural vibration control of base-isolated buildings using magnetorheological dampers, *J. Low Freq. Noise Vibr. Active Control* **37**(3) (2018) 565–576, doi: 10.1177/1461348417725959.
20. O. E. Ozbulut, P. N. Roschke, P. Y. Lin and C. H. Loh, GA-based optimum design of a shape memory alloy device for seismic response mitigation, *Smart Mater. Struct.* **19**(6) (2010) 065004, doi: 10.1088/0964-1726/19/6/065004.
21. Z. Lu, Z. Wang, S. F. Masri and X. Lu, Particle impact dampers: Past, present, and future, *Struct. Control Health Monitor.* **25**(1) (2018) e2058, doi: 10.1002/stc.2058.
22. Z. Zhao, R. Zhang and Z. Lu, A particle inerter system for structural seismic response mitigation. *J. Franklin Inst.* **356**(14) (2019) 7669–7688, doi: 10.1016/j.jfranklin.2019.02.001.
23. R. Zhang, Z. Zhao and K. Dai, Seismic response mitigation of a wind turbine tower using a tuned parallel inerter mass system, *Eng. Struct.* **180** (2019) 29–39, doi: 10.1016/j.engstruct.2018.11.020.
24. D. De Domenico, P. Deastra, G. Ricciardi and N. D. Sims, D. J. Wagg, Novel fluid inerter based tuned mass dampers for optimised structural control of base-isolated buildings. *J. Franklin Inst.* **356**(14) (2019) 7626–7649, doi: 10.1016/j.jfranklin.2018.11.012.
25. Y. Zheng, Y. Dong and Y. Li, Resilience and life-cycle performance of smart bridges with shape memory alloy (SMA)-cable-based bearings, *Construct. Build. Mater.* **158** (2018) 389–400, doi: 10.1016/j.conbuildmat.2017.10.031.
26. Y. Araki, K. Kimura, T. Asai, T. Masui, T. Omori and R. Kainuma, Integrated mechanical and material design of quasi-zero-stiffness vibration isolator with superelastic Cu–Al–Mn shape memory alloy bars, *J. Sound. Vibr.* **358** (2015) 74–83, doi: 10.1016/j.jsv.2015.08.018.
27. S. K. Mishra, S. Gur and S. Chakraborty, An improved tuned mass damper (SMA-TMD) (assisted by a shape memory alloy spring, *Smart Mater. Struct.* **22**(9) (2013) 095016, doi: 10.1088/0964-1726/22/9/095016.
28. M. Barbieri, S. Ilanko and F. Pellicano, Active vibration control of seismic excitation, *Nonlinear Dyn.* **93**(1) (2018) 41–52, doi: 10.1007/s11071-017-3853-y.
29. L. Xu, Y. Yu and Y. Cui, Active vibration control for seismic excited building structures under actuator saturation, measurement stochastic noise and quantisation, *Eng. Struct.* **156** (2018) 1–11, doi: 10.1016/j.engstruct.2017.11.021.
30. W. M. Zhong, X. X. Bai, C. Tang and A. D. Zhu, Principle study of a semi-active inerter featuring magnetorheological effect, *Frontiers Mater.* **6** (2019) 17, doi: 10.3389/fmats.2019.00017.
31. Y. Hu, M. Z. Q. Chen, S. Xu and Y. Liu, Semiactive inerter and its application in adaptive tuned vibration absorbers, *IEEE Trans. Control Syst. Technol.* **25**(1) (2017) 294–300, doi: 10.1109/TCST.2016.2552460.
32. M. Z. Q. Chen, Y. Hu, C. Li and G. Chen, Semi-active suspension with semi-active inerter and semi-active damper. *IFAC Proc. Vol.* **47**(3) (2014) 11225–11230, doi: 10.3182/20140824-6-ZA-1003.00138.

33. Z. M. Pawlak and R. Lewandowski, The effectiveness of the passive damping system combining the viscoelastic dampers and inerters, *Int. J. Struct. Stab. Dyn.* **20**(12) (2020) 2050140, doi: 10.1142/S0219455420501400.
34. H. N. Li, Z. Huang, X. Fu and G. Li, A re-centering deformation-amplified shape memory alloy damper for mitigating seismic response of building structures, *Struct. Control Health Monitor.* **25**(9) (2018) e2233, doi: 10.1002/stc.2233.
35. Y. Jia, L. Li, C. Wang, Z. Lu and R. Zhang, A novel shape memory alloy damping inerter for vibration mitigation, *Smart Mater. Struct.* **28**(11) (2019) 115002, doi: 10.1088/1361-665X/ab3dc8.
36. H. Huang, W. S. Chang and K. M. Mosalam, Feasibility of shape memory alloy in a tuneable mass damper to reduce excessive in-service vibration: Feasibility of shape memory alloy in a tuneable mass damper, *Struct. Control Health Monitor.* **24**(2) (2017) e1858, doi: 10.1002/stc.1858.
37. B. Wang and S. Zhu, Superelastic SMA U-shaped dampers with self-centering functions, *Smart Mater. Struct.* **27**(5) (2018) 055003, doi: 10.1088/1361-665X/aab52d.
38. Y. Jia, Z. Lu, L. Li and Z. Wu, A review of applications and research of shape memory alloys in civil engineering, *IOP Conf. Ser.: Mater. Sci. Eng.* **392** (2018) 022009, doi: 10.1088/1757-899X/392/2/022009.
39. P. S. Lobo, J. Almeida and L. Guerreiro, Shape memory alloys behaviour: A review, *Proc. Eng.* **114** (2015) 776–783, doi: 10.1016/j.proeng.2015.08.025.
40. J. Mohd Jani, M. Leary, A. Subic and M. A. Gibson, A review of shape memory alloy research, applications and opportunities, *Mater. Des. (1980–2015)* **56** (2014) 1078–1113, doi: 10.1016/j.matdes.2013.11.084.
41. H. Huang and W. S. Chang, Application of pre-stressed SMA-based tuned mass damper to a timber floor system, *Eng. Struct.* **167** (2018) 143–150, doi: 10.1016/j.engstruct.2018.04.011.
42. R. Li, H. Ge and G. Shu, Parametric study on seismic control design of a new type of SMA damper installed in a frame-type bridge pier, *J. Aerosp. Eng.* **31**(2) (2018) 04017100, doi: 10.1061/(ASCE)AS.1943-5525.0000809.
43. S. Pareek, Y. Suzuki, Y. Araki, M. A. Youssef and M. Meshaly, Plastic hinge relocation in reinforced concrete beams using Cu-Al-Mn SMA bars, *Eng. Struct.* **175** (2018) 765–775, doi: 10.1016/j.engstruct.2018.08.072.
44. Y. Araki, K. C. Shrestha, N. Maekawa, Y. Koetaka, T. Omori and R. Kainuma, Shaking table tests of steel frame with superelastic Cu–Al–Mn SMA tension braces, *Earthq. Eng. Struct. Dyn.* **45**(2) (2016) 297–314, doi: 10.1002/eqe.2659.
45. V. Torra, C. Auguet, G. Carreras, L. Dieng, F. C. Lovey and P. Terriault, The SMA: an effective damper in civil engineering that smoothes oscillations, *Mater. Sci. Forum* **706**–**709** (2012) 2020–2025, doi: 10.4028/www.scientific.net/MSF.706-709.2020.
46. H. Ma and C. Cho, Feasibility study on a superelastic SMA damper with re-centring capability, *Mater. Sci. Eng. A* **473**(1–2) (2008) 290–296, doi: 10.1016/j.msea.2007.04.073.
47. Y. Jia, Z. Lu, L. Li and C. Wang, A hybrid steel–shape memory alloy prestressed concrete beam for improved fire resistance, *Struct. Control Health Monitor.* **27**(10) (2020), doi: 10.1002/stc.2601.
48. S. Ghodke and R. S. Jangid, An empirical formulation for the damping ratio of shape memory alloy for base-isolated structures, *Int. J. Struct. Stab. Dyn.* **19**(7) (2019) 1950074, doi: 10.1142/S0219455419500743.
49. S. M. Yang, J. H. Roh, J. H. Han and I. Lee, Experimental studies on active shape control of composite structures using SMA actuators, *J. Intel. Mater. Syst. Struct.* **17**(8–9) (2006) 767–777, doi: 10.1177/1045389X06055830.

50. M. Formentini and S. Lenci, An innovative building envelope (kinetic façade) (with Shape Memory Alloys used as actuators and sensors, *Autom. Construct.* **85** (2018) 220–231, doi: 10.1016/j.autcon.2017.10.006.
51. C. Fang, M. C. H. Yam, A. C. C. Lam and L. Xie, Cyclic performance of extended end-plate connections equipped with shape memory alloy bolts, *J. Construct. Steel Res.* **94** (2014) 122–136, doi: 10.1016/j.jcsr.2013.11.008.
52. W. L. Cortés-Puentes and D. Palermo, Seismic retrofit of concrete shear walls with SMA tension braces, *J. Struct. Eng.* **144**(2) (2018) 04017200, doi: 10.1061/(ASCE)ST.1943-541X.0001936.
53. O. E. Ozbulut, S. Hurlebaus and R. Desroches, Seismic response control using shape memory alloys: A review. *J. Intel. Mater. Syst. Struct.* **22**(14) (2011) 1531–1549, doi: 10.1177/1045389X11411220.
54. Y. Araki, N. Maekawa, K. C. Shrestha, M. Yamakawa, Y. Koetaka and T. Omori *et al.*, Feasibility of tension braces using Cu-Al-Mn superelastic alloy bars, *Struct. Control Health Monitor.* **21**(10) (2014) 1304–1315, doi: 10.1002/stc.1644.
55. V. Torra, A. Isalgue, F. C. Lovey and M. Sade, Shape memory alloys as an effective tool to damp oscillations: study of the fundamental parameters required to guarantee technological applications, *J. Therm. Anal. Calorimet.* **119**(3) (2015) 1475–1533, doi: 10.1007/s10973-015-4405-7.
56. R. Zhang, Z. Zhao, C. Pan, K. Ikago and S. Xue, Damping enhancement principle of inerter system, *Struct. Control Health Monitor.* **27**(5) (2020) e2523, doi: 10.1002/stc.2523.
57. Y. Zhang, S. Jiang, L. Hu and Y. Liang, Deformation mechanism of NiTi shape memory alloy subjected to severe plastic deformation at low temperature, *Mater. Sci. Eng. A* **559** (2013) 607–614, doi: 10.1016/j.msea.2012.08.149.
58. X. W. Du, G. Sun and S. S. Sun, Piecewise linear constitutive relation for pseudo-elasticity of shape memory alloy (SMA), *Mater. Sci. Eng. A* **393**(1–2) (2005) 332–337, doi: 10.1016/j.msea.2004.11.018.
59. L. C. Brinson, One-dimensional constitutive behavior of shape memory alloys: Thermomechanical derivation with non-constant material functions and redefined martensite internal variable, *J. Intel. Mater. Syst. Struct.* **4**(2) (1993) 229–242, doi: 10.1177/1045389X9300400213.
60. X. Yan and J. Nie, Response of SMA superelastic systems under random excitation, *J. Sound. Vibr.* **238**(5) (2000) 893–901, doi: 10.1006/jsvi.2000.3020.
61. Y. K. Wen, Method for random vibration of hysteretic systems,*J. Eng. Mech. Div.* **102**(2) (1976) 249–263.
62. E. J. Graesser and F. A. Cozzarelli, Shape-memory alloys as new materials for aseismic isolation, *J. Eng. Mech.* **117**(11) (1991) 2590–2608, doi: 10.1061/(ASCE)0733-9399(1991)117:11(2590).
63. R. Wang, K. Yasuda and Z. Zhang, A generalized analysis technique of the stationary FPK equation in nonlinear systems under Gaussian white noise excitations, *Int. J. Eng. Sci.* **38**(12) (2000) 1315–1330, doi: 10.1016/S0020-7225(99)00081-6.
64. J. E. Hurtado and A. H. Barbat, Equivalent linearization of the Bouc–Wen hysteretic model, *Eng. Struct.* **22**(9) (2000) 1121–1132, doi: 10.1016/S0141-0296(99)00056-5.
65. W. Q. Zhu, Z. L. Huang and Y. Suzuki, Equivalent non-linear system method for stochastically excited and dissipated partially integrable Hamiltonian systems, *Int. J. Non-Linear Mech.* **36**(5) (2001) 773–786, doi: 10.1016/S0020-7462(00)00043-3.
66. A. de Lataillade, S. Blanco, Y. Clergent, J. L. Dufresne, M. El Hafi and R. Fournier, Monte Carlo method and sensitivity estimations, *J. Quant. Spectrosc. Radiat. Transf.* **75**(5) (2002) 529–538, doi: 10.1016/S0022-4073(02)00027-4.

67. T. Liu, T. Zordan, B. Briseghella and Q. Zhang, Evaluation of equivalent linearization analysis methods for seismically isolated buildings characterized by SDOF systems, *Eng. Struct.* **59** (2014) 619–634, doi: 10.1016/j.engstruct.2013.11.028.
68. F. R. Rofooei, A. Mobarake and G. Ahmadi, Generation of artificial earthquake records with a nonstationary Kanai–Tajimi model, *Eng. Struct.* **23**(7) (2001) 827–837, doi: 10.1016/S0141-0296(00)00093-6.
69. P. Brzeski, T. Kapitaniak and P. Perlikowski, Novel type of tuned mass damper with inerter which enables changes of inertance, *J. Sound. Vibr.* **349** (2015) 56–66, doi: 10.1016/j.jsv.2015.03.035.
70. C. Pan, R. Zhang, H. Luo and H. Shen, Target-based algorithm for baseline correction of inconsistent vibration signals, *J. Vibr. Control* **24**(12) (2018) 2562–2575, doi: 10.1177/1077546316689014.
71. C. Pan, R. Zhang, H. Luo and H. Shen, Baseline correction of vibration acceleration signals with inconsistent initial velocity and displacement, *Adv. Mech. Eng.* **8**(10) (2016) 168781401667553, doi: 10.1177/1687814016675534.